

# X-Ray Structure of the Pestivirus NS3 Helicase and Its Conformation in Solution

M. Alejandra Tortorici,<sup>a,b</sup> Stéphane Duquerroy,<sup>a,b,c</sup> Jane Kwok,<sup>a,d</sup> Clemens Vornrhein,<sup>e</sup> Javier Perez,<sup>f</sup> Benjamin Lamp,<sup>g</sup> Gerard Bricogne,<sup>e</sup> Till Rümenapf,<sup>g</sup> Patrice Vachette,<sup>h</sup> Félix A. Rey<sup>a,b</sup>

Unité de Virologie Structurale, Département de Virologie, Institut Pasteur, Paris, France<sup>a</sup>; CNRS, UMR 3569, Paris, France<sup>b</sup>; Université Paris Sud, Gif sur Yvette, France<sup>c</sup>; Department of Physiology, Li Ka Shing Faculty of Medicine, University of Hong Kong, Hong Kong<sup>d</sup>; Global Phasing Ltd., Cambridge, United Kingdom<sup>e</sup>; Synchrotron Soleil, Gif sur Yvette, France<sup>f</sup>; Institute of Virology, University of Veterinary Medicine, Vienna, Austria<sup>g</sup>; Institut de Biologie Intégrative de la Cellule, UMR 9198, Gif-sur-Yvette, France<sup>h</sup>

## ABSTRACT

Pestiviruses form a genus in the *Flaviviridae* family of small enveloped viruses with a positive-sense single-stranded RNA genome. Viral replication in this family requires the activity of a superfamily 2 RNA helicase contained in the C-terminal domain of nonstructural protein 3 (NS3). NS3 features two conserved RecA-like domains (D1 and D2) with ATPase activity, plus a third domain (D3) that is important for unwinding nucleic acid duplexes. We report here the X-ray structure of the pestivirus NS3 helicase domain (pNS3h) at a 2.5-Å resolution. The structure deviates significantly from that of NS3 of other genera in the *Flaviviridae* family in D3, as it contains two important insertions that result in a narrower nucleic acid binding groove. We also show that mutations in pNS3h that rescue viruses from which the core protein is deleted map to D3, suggesting that this domain may be involved in interactions that facilitate particle assembly. Finally, structural comparisons of the enzyme in different crystalline environments, together with the findings of small-angle X-ray-scattering studies in solution, show that D2 is mobile with respect to the rest of the enzyme, oscillating between closed and open conformations. Binding of a nonhydrolyzable ATP analog locks pNS3h in a conformation that is more compact than the closest apo-form in our crystals. Together, our results provide new insight and bring up new questions about pNS3h function during pestivirus replication.

## IMPORTANCE

Although pestivirus infections impose an important toll on the livestock industry worldwide, little information is available about the nonstructural proteins essential for viral replication, such as the NS3 helicase. We provide here a comparative structural and functional analysis of pNS3h with respect to its orthologs in other viruses of the same family, the flaviviruses and hepatitis C virus. Our studies reveal differences in the nucleic acid binding groove that could have implications for understanding the unwinding specificity of pNS3h, which is active only on RNA duplexes. We also show that pNS3h has a highly dynamic behavior—a characteristic probably shared with NS3 helicases from all *Flaviviridae* members—that could be targeted for drug design by using recent algorithms to specifically block molecular motion. Compounds that lock the enzyme in a single conformation or limit its dynamic range of conformations are indeed likely to block its helicase function.

Pestiviruses infect a wide range of cloven-hoofed animals, wild and domestic, causing serious disease. The most studied are the classical swine fever virus (CSFV) (1) and the bovine viral diarrhea virus (BVDV), which impose important economic losses to the livestock industry worldwide (2). They form a genus within the *Flaviviridae* family of single-stranded RNA viruses, which also includes medically important pathogens in the flavi- and hepacivirus genera. Recent studies also revealed that hepacivirus and pegivirus (the fourth genus in the family) cause infections in horses and other domestic animals (3, 4).

The pestivirus genome is a single mRNA molecule of about 12.3 kb with a single large open reading frame (ORF) coding for a polyprotein precursor of about 3,900 residues. This long ORF is flanked by 5' and 3' untranslated regions with *cis*-active elements essential for virus translation and replication (2). The polyprotein is co- and posttranslationally processed by cellular and virus genome-encoded proteases to yield the individual mature viral proteins in the order shown in Fig. 1A (2, 5, 6). Structural studies are available for nonstructural protein 5B (NS5B) (7), E<sup>ns</sup> (8), E2 (9, 10), and N<sup>pro</sup> (11, 12). N<sup>pro</sup> and E<sup>ns</sup> are unique to pestiviruses, while all the others have their counterparts in the other genera.

Particle morphogenesis in the infected cell occurs when the core protein forms a ribonucleoprotein (RNP) complex with the genomic RNA, which then buds into the lumen of an internal compartment, thereby acquiring a lipid envelope in which are incorporated the three envelope proteins E<sup>ns</sup>, E1, and E2. The nonstructural proteins NS2 through NS5B are present only in

Received 30 October 2014 Accepted 27 January 2015

Accepted manuscript posted online 4 February 2015

Citation Tortorici MA, Duquerroy S, Kwok J, Vornrhein C, Perez J, Lamp B, Bricogne G, Rümenapf T, Vachette P, Rey FA. 2015. X-ray structure of the pestivirus NS3 helicase and its conformation in solution. *J Virol* 89:4356–4371. doi:10.1128/JVI.03165-14.

Editor: M. S. Diamond

Address correspondence to M. Alejandra Tortorici, tortorici@pasteur.fr, or Félix A. Rey, rey@pasteur.fr.

Supplemental material for this article may be found at <http://dx.doi.org/10.1128/JVI.03165-14>.

Copyright © 2015, American Society for Microbiology. All Rights Reserved. doi:10.1128/JVI.03165-14

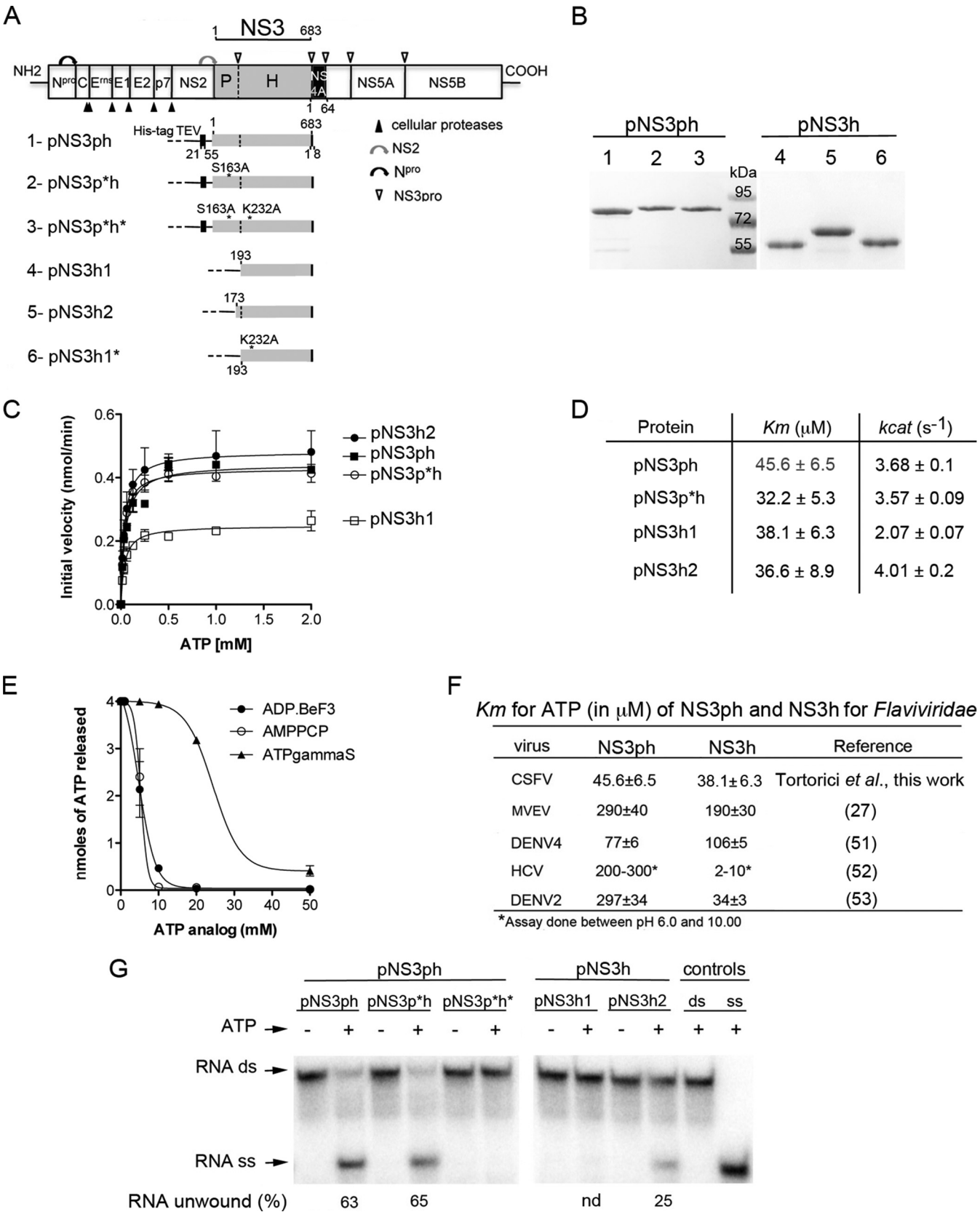


FIG 1 Biochemical characterization of recombinant pNS3 and pNS3h from CSFV. (A) Schematic diagram of the pestivirus precursor polyprotein organization, indicating the individual mature proteins (boxes) and proteolytic processing sites (arrowheads or curved arrows for autoproteolytic cleavages). A diagram of the different constructs used in this study is shown below. (B) SDS-PAGE analysis of purified recombinant proteins stained with Coomassie blue. The lanes labeled

infected cells and are essential for virus replication. Among them, NS2 (a cysteine protease), NS5B (the RNA-dependent RNA polymerase), and NS3 have enzymatic activities. NS3 has a molecular mass of about 76 kDa and features two main functional domains, each with different enzymatic activities. The N-terminal domain is a chymotrypsin-like serine protease, which is responsible for most of the maturation cleavages of the polyprotein precursor in the cytosolic side of the endoplasmic reticulum membrane (Fig. 1A); the exception is the NS2/NS3 junction (2). The C-terminal domain, about two-thirds of NS3, is a helicase belonging to superfamily 2 (SF2) that displays characteristic sequence motifs that constitute the SF2 signature (13). The helicase activity is thought to be important for unwinding highly structured regions of the RNA genome during replication. While NS3 from hepatitis C virus (HCV) unwinds both RNA and DNA double-stranded helices, pesti- and flavivirus helicases unwind only RNA duplexes (14, 15). The protease and helicase domains of NS3 (NS3p and NS3h, respectively) are believed to function at different stages of the replication cycle, although in the case of HCV, the two domains were shown to enhance each other's activities (16, 17). NS3 was recently shown to be autoproteolyzed in CSFV-infected cells to release NS3h (6). In addition, NS3 was shown to play other functions in the virus cycle, such as interfering with the innate immune system in the case of HCV (18) and modulating fatty acid synthesis in the case of dengue virus (DENV) (19). It was also shown to participate in genome packaging and particle assembly in HCV (20, 21), yellow fever virus (22, 23), and pestiviruses (24). Indeed, an apparent interplay between genomic RNP formation and interactions with NS3 has been reported: CSFV virions lacking the core protein were found to be viable only when NS3 is mutated at specific locations.

Studies on HCV and several flaviviruses have provided important insight into the translocation mechanism of NS3 along nucleic acid polymers (25–30), but very little is known about the pestivirus counterpart (15, 31). For clarity, here we use “pNS3” to specify the pestivirus enzyme. No three-dimensional (3D) structure is available for pNS3, except for a homology model based on HCV NS3h that was recently published (32). Given that the amino acid sequence identity between NS3 from HCV and the pestiviruses is low (less than 20%), the relevance of the proposed 3D model remains to be tested.

We report here an enzymatic characterization and the X-ray structure of the pNS3 helicase domain (pNS3h) from CSFV. We found that pNS3p or portions of it modulate the unwinding activity of pNS3, as is the case for NS3 from the other genera. The crystal structure showed that the RecA-like pNS3h domains D1 and D2 are quite similar to those of HCV and DENV NS3h. In contrast, there are important differences in the nucleic acid binding groove (NABG), which result from two insertions in D3. Furthermore, the various reported mutations affecting pestivirus

genomic RNA encapsidation map to D3, although they do not make a specific surface patch or affect the RNA unwinding activity of pNS3. Our crystallographic analyses, together with small-angle X-ray-scattering (SAXS) experiments in solution, further show that pNS3h has a highly dynamic behavior that is in line with its expected motor-like translocation activity along the pestivirus RNA genome.

## MATERIALS AND METHODS

**Cloning, expression, and purification.** The oligonucleotide sequences used in this study are displayed in Table S1 in the supplemental material. To express pNS3h we modified the construct described previously (6) by introducing the tobacco etch virus (TEV) protease cleavage site (ENLY FQG) between a histidine (His) tag and the beginning of the pNS3h sequence to have the ability to remove the N-terminal His tag. The resulting vector allows the expression of pNS3h1, which is a 516-residue protein comprising pNS3 residues 193 to 683 (corresponding to residues 1782 to 2272 in the polyprotein) fused to a His tag plus the TEV protease cleavage site at the N terminus and the first 8 residues of NS4A at the C terminus (Fig. 1A). We also modified this construct to express pNS3h2, a 536-residue protein comprising pNS3 (residues 173 to 683) (33). To express full-length pNS3ph, we used the construct described elsewhere (6), which includes the NS3-activating sequence of NS4A (residues 21 to 55) fused to the N terminus of NS3 (residues 1 to 683) through a GSGS linker. As for the pNS3h constructs, the His tag plus the TEV site and the first 8 residues of NS4A were fused to the N and C termini, respectively. All the mutations that we describe in this work were introduced into the corresponding plasmids by outward PCR. Identical protocols were used to express and purify all the proteins used in this study. Transformed *Escherichia coli* Rosetta(DE3)pLysS cells (Novagen) were grown at 37°C in Luria-Bertani medium (LB) containing 100 mg ml<sup>-1</sup> ampicillin, 35 mg ml<sup>-1</sup> chloramphenicol, and 0.3% glucose to an optical density at 600 nm of 0.6 to 0.8. Protein expression at 30°C was induced with 1 mM isopropyl-β-D-1-thiogalactopyranoside. Selenomethionine (SeMet)-labeled pNS3h protein was expressed in *E. coli* strain B834(DE3) (Novagen), a methionine auxotroph, in a deep liver medium (DLM) containing 0.2 g liter<sup>-1</sup> SeMet. After 4 h induction, the cells were harvested by centrifugation and stored at -80°C. Frozen cells pellets from a 1-liter culture were resuspended in 40 ml of lysis buffer (50 mM NaHPO<sub>4</sub>, pH 7.5, 300 mM NaCl, 1% Triton X-100, 2 mM dithiothreitol [DTT], 40 mM imidazole) supplemented with a protease inhibitor cocktail (Complete, EDTA free; Roche) and lysed by high pressure using an EmulsiFlex-C5 homogenizer (Avestin). The lysate was clarified by centrifugation at 30,000 × g for 30 min at 4°C. The supernatant was filtered (pore size, 0.22 μm; Millipore), loaded onto a nickel-affinity resin (His-Trap HP; GE Healthcare), washed with 50 mM NaHPO<sub>4</sub>, pH 7.5, 300 mM NaCl, 40 mM imidazole, and eluted with a 40 to 500 mM imidazole gradient. Fractions containing His-tagged protein were pooled and loaded into a gel filtration column (Superdex 200; GE Healthcare) that had previously been equilibrated in 20 mM Tris-HCl, pH 7.5, 100 mM NaCl, 2 mM DTT. The His tag was removed by TEV cleavage in a reaction mixture containing His-tagged pNS3h and His-tagged TEV at a molar ratio of 1:3 in TEV buffer (50 mM Tris-HCl [pH 8.0], 0.5 mM EDTA, and 1 mM DTT). The reaction mix was incubated at 4°C overnight and reloaded into a His-Trap column to remove uncleaved protein and

1 through 6 correspond to the various constructs listed in panel A. The middle lane displays prestained molecular mass markers. (C) The ATP hydrolysis activity of the proteins was measured by determination of the release of inorganic phosphate (y axis) and was plotted as a function of the ATP concentration (x axis). (D) Summary of the ATP hydrolysis properties of the different pNS3ph and pNS3h constructs. (E) The ATPase rate was measured in the presence of 0.2 mM ATP and the indicated concentrations of nonhydrolyzable ATP analogs (ADP-BeF<sub>3</sub>, AMPPCP, and ATPγS). Plotted is the amount of hydrolyzed ATP (y axis) against the ATP analog concentration (x axis). The standard deviations in panels C and E were estimated from two independent experiments. (F) The *K<sub>m</sub>* for ATP hydrolysis was determined by fitting the data from panel C with the Michaelis-Menten equation and is presented here in comparison to the corresponding values obtained for NS3 of other *Flaviviridae* members available in the literature. (G) The unwinding activities of pNS3ph and pNS3h were measured under multiple turnover assay conditions. The percentage of unwound RNA was calculated by dividing the amount of single-stranded RNA (RNA ss) by the total amount of RNA (single-stranded RNA plus double-stranded [RNA ds]). nd, not detected.

the tagged TEV protease. The cleaved protein was further purified on a gel filtration column as described above for the tagged protein. The samples were kept at 4°C until concentration to about 6 to 7 mg ml<sup>-1</sup> on a Vivaspin apparatus, performed immediately before the crystallization trials.

**ATPase assay.** The steady-state rate of ATP hydrolysis was measured by determining the release of inorganic phosphate, initially by using radioactive [ $\gamma$ -<sup>32</sup>P]ATP and, later, for more accurate results at high ATP concentrations (Fig. 1C), by using a colorimetric assay from Innova Biosciences following the manufacturer's instructions. Briefly, 10 nM protein was incubated with different amounts of ATP in ATPase buffer [50 mM Tris-HCl, pH 7.5, 2.5 mM MgCl<sub>2</sub>, 50 mM NaCl, 1 mM tris(2-carboxyethyl) phosphine (TCEP)] for 15 min at room temperature. The absorbance at 630 nm was converted to the inorganic phosphate concentration using a standard curve. The  $K_m$  and the turnover number ( $k_{cat}$ ) of the enzymes were determined from measurements of the initial rates at different ATP concentrations with GraphPad Prism software.

**Screening of ATP analogs by inhibition of ATPase activity.** For screening the effect of ATP analogs (Fig. 1E), we used a radioactivity assay. Briefly, pNS3h (0.33  $\mu$ M) was incubated for 15 min at room temperature in a 20- $\mu$ l reaction mixture in ATPase buffer containing 1  $\mu$ Ci/ $\mu$ l of [ $\gamma$ -<sup>32</sup>P]ATP (3,000 Ci/mmol), 200  $\mu$ M cold ATP, and different concentrations (0.5 to 50 mM) of ground-state ATP analogs, such as ADP-BeF<sub>3</sub>,  $\beta$ , $\gamma$ -methyleneadenosine 5'-triphosphate (AMPPcP), and adenosine 5'-( $\gamma$ -thio) triphosphate (ATP $\gamma$ S). One-microliter aliquots were spotted onto polyethylenimine-cellulose membranes (Merck), and the reaction products were resolved by ascending thin-layer chromatography in 1 M formic acid–0.5 M LiCl. Radiolabeled spots on the membranes were detected by autoradiography and quantified with a phosphorimager.

**Unwinding assays.** To generate substrates for helicase assays, two synthetic oligonucleotides were annealed in 50 mM Tris-HCl, pH 8.0, 55 mM KCl, and 5 mM MgCl<sub>2</sub> by heating to 95°C and allowing them to cool slowly to room temperature. Before annealing, the shorter strand of the duplex substrate was <sup>32</sup>P labeled using polynucleotide kinase. The duplex DNA substrate consisted of the shorter DNA oligonucleotide (5'-[<sup>32</sup>P]GCCTCGCTGCCGTCGCCA-3') annealed to the longer DNA oligonucleotide (5'-TGGCGACGGCAGCGAGGCTTTTTTTTTTTT-3'). The duplex RNA substrate consisted of the shorter RNA oligonucleotide (5'-[<sup>32</sup>P]CGACUCUAGAGAGGUG-3') annealed to the longer RNA oligonucleotide (5'-CACCUCUCUAGAGUGCAGGCAUCG-3'). The DNA or RNA substrate (5 nM) and 400 nM protein were incubated in 20- $\mu$ l reaction mixtures including 25 mM sodium phosphate buffer, pH 7.5, 1 mM DTT, 3 mM MgCl<sub>2</sub>, 0.1 mg ml<sup>-1</sup> bovine serum albumin, and 3 U RNasin (RNase inhibitor) for 15 min at 25°C. Reactions were initiated by the addition of 5 mM ATP and terminated by the addition of 5  $\mu$ l of loading buffer (20 mM Tris-HCl, pH 7.5, 4 mM EDTA, 0.1% SDS, 50% glycerol, 0.01% bromophenol blue, 0.01% xylene cyanol) after 30 min at 37°C. Multiple turnover unwinding reactions were performed by adding 5  $\mu$ M excess unlabeled short DNA or RNA oligonucleotide as an enzyme trap at the end of the reaction. Reaction products were separated by electrophoresis on a 10% acrylamide native gel and detected and quantified with a phosphorimager.

**Crystallization and structure determination.** Crystals of native pNS3h (wild type or mutant) and the SeMet-substituted protein were grown at 20°C by vapor diffusion under the conditions listed in Table 1. For data collection, the crystals were flash cooled in liquid nitrogen using 20% glycerol as a cryoprotectant. Diffraction data were collected at synchrotron beam line PX1 of the Swiss Light Source (SLS X06SA) using a Pilatus 6M detector (34, 35). Our initial attempts to determine the structure by molecular replacement using the available models of NS3h from HCV or the flaviviruses failed. We therefore grew crystals of SeMet-substituted protein to obtain experimental phases. These correspond to crystal form 2 (Table 1). As pNS3h has 21 methionines, the 4 molecules in the asymmetric unit (AU) amounted to 84 selenium sites, the coordinates of which needed to be determined to calculate phases. This required an *ad hoc* data collection strategy to measure anomalous and dispersive pairs of

reflections as close in time as possible to minimize errors introduced by radiation damage. We collected the required diffraction data in 5-degree slices in inverse beam mode and switched wavelengths between the peak and the inflection points of the absorption edge within each slice. The diffraction data were indexed and processed with the XDS program suite (36) (the MOSFLM program was used for visualizing the indexing) and scaled using SCALA software (37). The program SHELXC was used to estimate heavy atom structure factors from the 2-wavelength anomalous dispersion data (peak and inflection). These data were then used in the SHELXD program to a resolution of 5 Å to find the Se sites. On purpose, a much lower estimate of the number of sites was used (21 out of 84 sites in the 4 molecules of the AU), since initial trials using the full number of expected sites were unsuccessful. Those initial 21 sites were used in the SHARP program for parameter refinement and calculation of log-likelihood gradient (LLG) residual maps. Inspection of the resulting electron density maps allowed the identification of further sites, and this was followed by additional SHARP runs. Iterating these steps gave a final heavy atom model containing 66 sites. Density modification using the SOLOMON program gave a partially interpretable map using a solvent content of 52%. The density-modified map was used in the Buccaneer program (38) to build an initial model of 1,536 residues corresponding to the 4 molecules of the AU. The best map from auto-SHARP was used as a starting point in 2-fold noncrystallographic symmetry (NCS) averaging with the DM program (39). The program Buccaneer was then able to build 1,841 residues (out of 2,064 residues) into the 2-fold averaged map, with most of them being assigned in sequence correctly. The model was subsequently manually modified with the Coot program (40) and refined with the BUSTER-TNT program (41). This atomic model was then used for molecular replacement with the AMoRe program (42) to determine the structures of pNS3h in crystals forms 1 and 3, as well as crystals 4 and 5 (corresponding to the N588Y and Q600K mutants, respectively).

**Normal modes analysis (NMA).** To analyze the transition between the various conformations of pNS3h observed in the crystals, we used the two extreme conformations observed in the AU of crystal form 2 to calculate normal modes with the NOMAD-Ref and eNemo (<http://www.sciences.univ-nantes.fr/elnemo/>) servers (43, 44). The programs compute the low-frequency normal modes for a given protein structure, suggesting potential conformational changes.

**Small-angle X-ray scattering.** X-ray-scattering data were collected at the SWING and ID14-3 beamlines of the Soleil synchrotron (Saint Aubin, France) and the European Synchrotron Radiation Facility (ESRF; Grenoble, France), respectively. The SWING data were recorded with a charge-coupled-device-based detector (AVIEX) at an X-ray wavelength ( $\lambda$ ) of 1.033 Å at 15°C on TEV protease-treated pNS3h to remove the His tag. We did the measurements over a range of protein concentrations ranging from 0.5 to 8 mg ml<sup>-1</sup> in SAXS buffer (20 mM Tris-HCl, pH 7.5, 100 mM NaCl) with the addition of either 5 mM TCEP (Pierce) or 2 mM DTT. The samples were circulated through a 1.8-mm-diameter quartz capillary using an automatic sample changer (Agilent). In addition, we also made measurements using 40  $\mu$ l of an 8-mg ml<sup>-1</sup> solution of pNS3h loaded onto a Superdex 200 size exclusion column mounted on a high-pressure liquid chromatography (HPLC) system (Agilent) online with an SAXS measuring cell (size exclusion chromatography [SEC]-SAXS) (45). The absorbance at 280 nm in the elution profile exhibited only a faint trace of small oligomers (representing about 2% of the total protein in solution) before the peak corresponding to the monomeric fraction (data not shown). In both cases, the flow rate was high enough to minimize radiation damage. The resulting data were processed with the PRIMUS package (46). The forward scattering [ $I(0)$ ] and the radius of gyration ( $R_g$ ) were evaluated using the Guinier approximation (47). Frames over the elution peak recorded using the size exclusion HPLC were analyzed individually before averaging the appropriate subset, yielding identical  $R_g$  and  $I(0)/c$  (where  $c$  is the protein concentration) values. The most concentrated samples were used to measure scattering data only at higher angles because the curve exhibited distortions at small  $q$  values ( $q = 4\pi \sin \theta/\lambda$  or



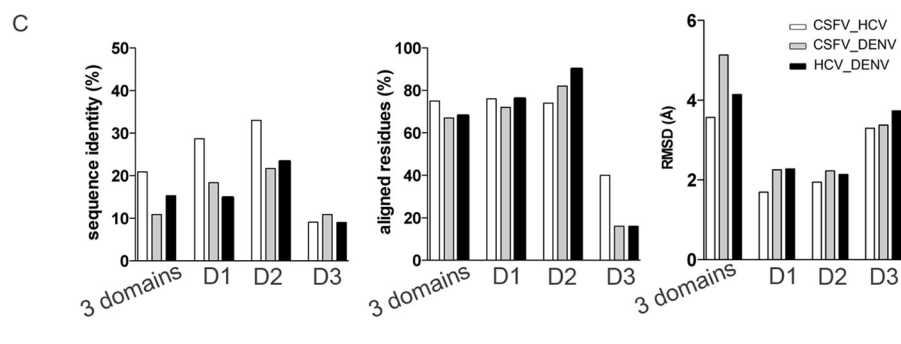
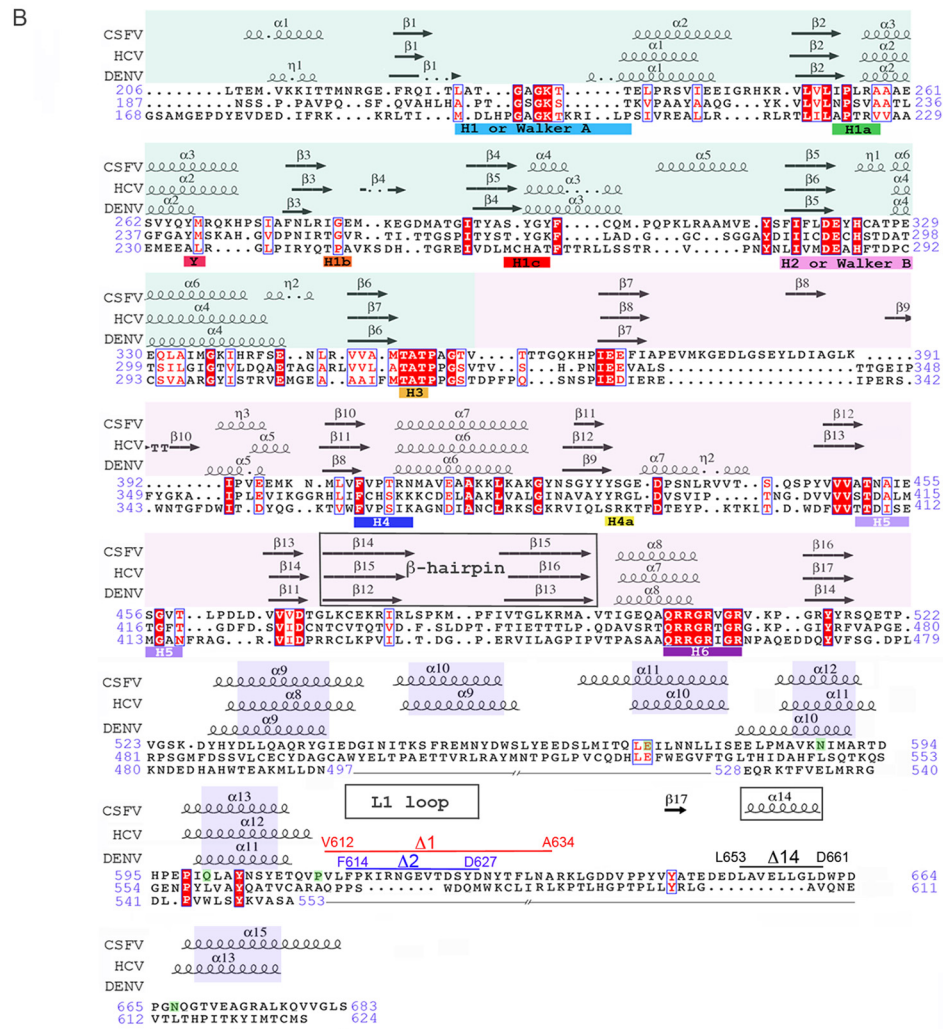
TABLE 1 Crystallographic statistics for CSFV NS3h crystal forms<sup>a</sup>

Parameter	Value for the following crystal:				
	Crystal form 1	Crystal form 2	Crystal form 3	N588Y crystal	Q600K crystal
PDB accession no.	<b>4CBH</b>	<b>4CBG</b>	<b>4CBI</b>	<b>4CBL</b>	<b>4CBM</b>
Crystallization conditions	0.1 M Na cacodylate, pH 6.5, 0.2 M magnesium acetate, 12% PEG 8000	1 M Na cacodylate, pH 6.5, 0.2 M magnesium acetate, 12% PEG 8000	0.1 M MES, pH 6.5, 0.6 M NaCl, 20% PEG 4000, 1 mM AMPPcP <sup>b</sup>	0.1 M Na cacodylate, pH 6.5, 0.15 M calcium acetate, 12% PEG 3350	0.1 M NaAc, pH 4.6, 0.025 M calcium acetate, 9% PEG 4000
Data collection statistics					
Space group	P2 <sub>1</sub>	P2 <sub>1</sub>	P1	P2 <sub>1</sub>	P2 <sub>1</sub>
Unit cell dimensions <i>a</i> , <i>b</i> , <i>c</i> (Å)	70.07, 144.4, 118.690	70.455, 168.360, 98.8	69.63, 96.303, 97.611	70.027, 156.820, 99.52	70.1, 159.585, 99.227
$\alpha = \beta = \gamma$ (°)	92.94	98.522	91.23, 110.86, 107.62	97.39	97.24
Resolution range (Å)	44.34–2.51 (2.58–2.51)	49.57–2.82 (2.89–2.82)/49.57–2.98 (3.16–2.98) <sup>c</sup>	46.83–3.00 (3.16–3.00)	39.21–3.05 (3.21–3.05)	37.98–3.27 (3.45–3.27)
No. of reflections					
Measured	277,586	402,065/192,825 <sup>c</sup>	84,132	208,052	77,233
Unique	71,319	49,724/43,835 <sup>c</sup>	40,172	38,441	31,533
Completeness (%)	88.63	91.5/96.4 <sup>c</sup>	89.8	94.9	94.4
Multiplicity	4.0 (2.3)	8.1 (3.4)/4.4 (2.1) <sup>c</sup>	2.1 (1.9)	5.4 (4.1)	2.4 (1.8)
<i>I</i> / $\sigma$ <i>I</i>	15.4 (2.0)	16.2 (2.0)/12.2 (1.9) <sup>c</sup>	7.2 (1.7)	10.4 (1.8)	7.0 (1.9)
<i>R</i> <sub>merge</sub> (%) <sup>d</sup>	6.9 (39)	13.3 (34.9)/11.8 (23.4) <sup>c</sup>	8.9 (40.9)	12.3 (64.5)	2.8 (55.4)
<i>R</i> <sub>anom</sub> (%) <sup>e</sup>		8.2 (28.4)/7.6 (24.1) <sup>c</sup>			
Anomalous completeness (%)		87.2 (58.3)/85.1 (50.3) <sup>c</sup>			
Anomalous signal up to the indicated resolution (Å)		3.99/5.15 <sup>c</sup>			
Refinement statistics					
No. of reflections in refinement (free)	71,319 (3,572)	49,698 (2,532)	40,150 (1,996)	33,223 (1,647)	31,359 (1,585)
No. of molecules per asymmetric unit	4	4	4	4	4
<i>R</i> <sub>work</sub> (%) <sup>f</sup>	20.41	16.61	19.21	24.6	23.30
<i>R</i> <sub>free</sub> (%) <sup>f</sup>	23.75	20.49	24.67	25.66	27.0
No. of:					
Protein atoms	11,032	14,731	13,820	14,530	14,595
Water molecules	928	122	105	0.007	0.01
RMSD					
Bond length (Å)	0.010	0.01	0.01	1.0	1.12
Bond angle (°)	1.28	1.19	1.21	79.0	64.57
Overall avg B factor (Å <sup>2</sup> )	60.78	66.05	65.06	95.81	96.1
Ramachandran plot (%) <sup>g</sup>	97.4		96.24	3.05	3.18
Favored regions	1.93	97.14	2.85	1.13	0.72
Allowed regions	0.67	2.26	0.9		
Outlier regions		0.6			

<sup>a</sup> Data in parentheses are for the last shell. PEG, polyethylene glycol; MES, morpholineethanesulfonic acid; NaAc, sodium acetate.<sup>b</sup> No electron density corresponding to AMPPcP was found in crystal form 3.<sup>c</sup> Data are those for the peak point/inflection point.<sup>d</sup>  $R_{\text{merge}} = \sum (\sum |I_i - \langle I \rangle| / \sum |I|)$ , where the first  $\sum$  is the sum over all reflections, and the second  $\sum$  is the sum over all measurements of a given reflection, with  $I_i$  being the *i*th measurement of the intensity of the reflection and  $\langle I \rangle$  the average intensity of that reflection.<sup>e</sup>  $R_{\text{anom}} = \sum |\text{Mn}(I^+) - \text{Mn}(I^-)| / \sum [\text{Mn}(I^+) + \text{Mn}(I^-)]$ , where  $I$  is intensity and the + and – correspond to the Friedel-Bijvoet pair for the same  $I$ , summed over all reflections.<sup>f</sup>  $R_{\text{work}}/R_{\text{free}} = \sum (|F_o| - \langle |F_c| \rangle) / \sum |F_o|$ , where  $\langle |F_c| \rangle$  is the expectation of  $|F_c|$  under the probability model used to define the likelihood function. The sum is overall reflections.<sup>g</sup> Calculated by use of the MolProbity program.

momentum transfer, where  $2\theta$  is the scattering angle and  $\lambda$  is the wavelength of the X rays), with a Guinier plot yielding an apparent  $R_g$  value of 31.8 Å (which was 15% higher than the value from the SEC-SAXS data). This was due to the presence of the small amount of oligomers revealed by

gel filtration and to the existence of attractive interactions between molecules at a high concentration. Therefore, the average curve from the SEC-SAXS data was spliced with that for the most concentrated sample (after scaling to the same protein concentration) to yield a complete scat-



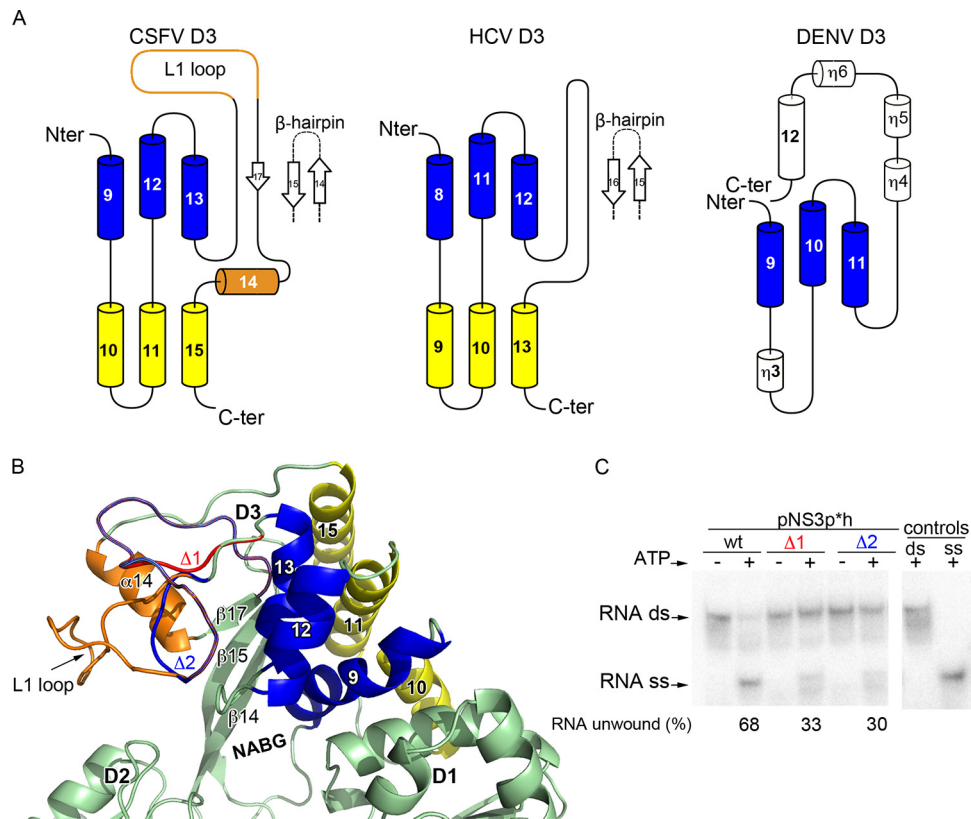


**FIG 3** Domain 3 comparison with its NS3h orthologs. (A) Topology diagram of *Flaviviridae* NS3h domain 3. In pNS3h D3, the common core of three  $\alpha$  helices shared with HCV and DENV NS3h is shown in blue, and the additional three  $\alpha$  helices shared between CSFV and HCV D3 are shown in yellow. The secondary structure elements are numbered according to the structural alignment shown in Fig. 2. (B) Zoom view of CSFV NS3h D3. The  $\alpha$  helices shared with HCV and DENV are shown using the same color code used for panel A. The two insertions in pNS3h D3, the L1 loop and helix  $\alpha$ 14, are colored orange. (C) Unwinding activity of pNS3, using construct pNS3p<sup>h</sup> and the deletion mutants  $\Delta$ 1 and  $\Delta$ 2 (see Fig. 2B), measured using an RNA duplex template. The percentage of unwound RNA was calculated as described in the legend to Fig. 1.

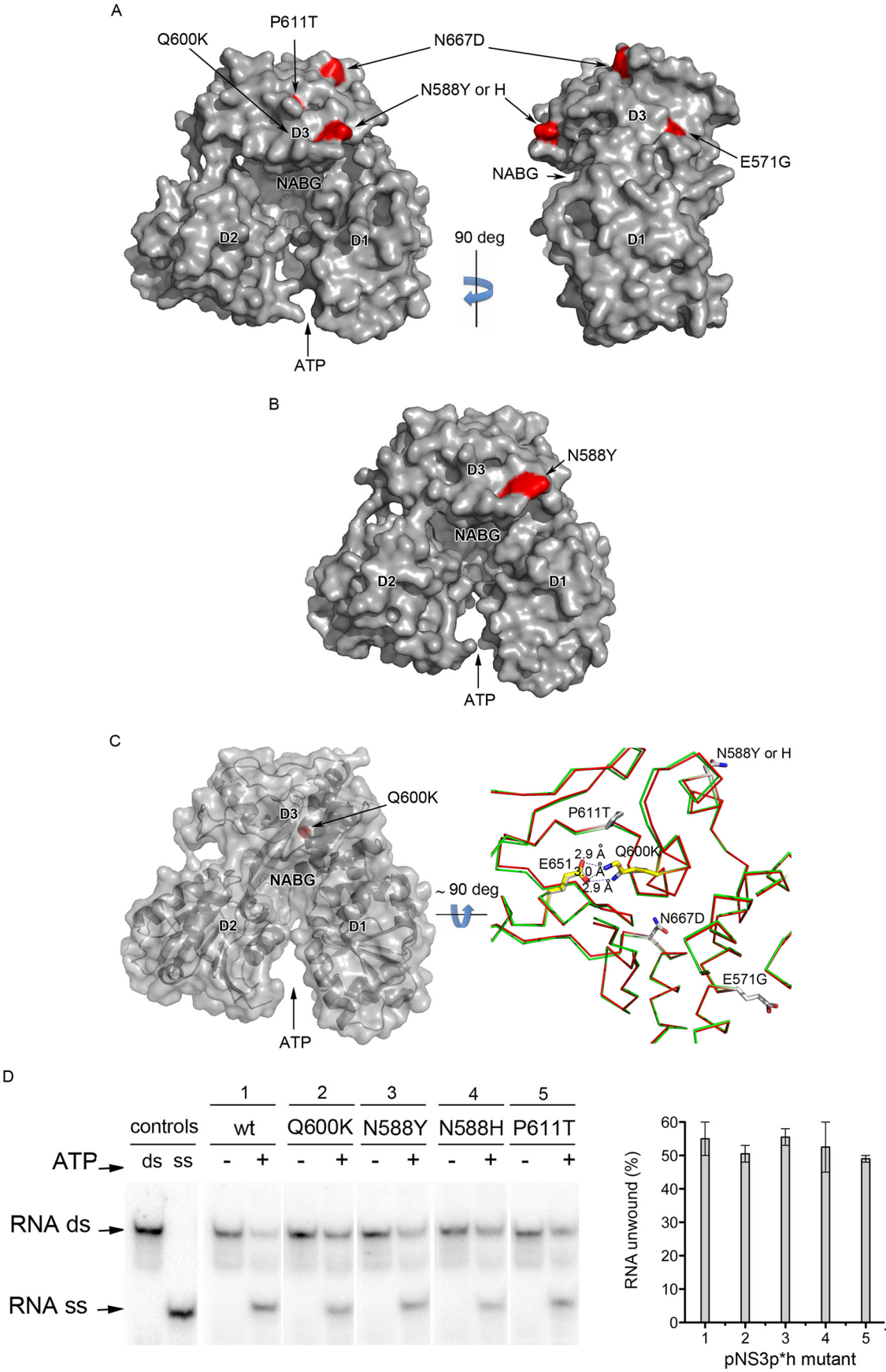
tering curve (see Fig. S1A in the supplemental material). The pair distance distribution function  $[p(r)]$  was determined using the indirect Fourier transform method implemented in the program GNOM (48). The molecular mass of the protein was evaluated by comparison of the forward scattering with that of water recorded in the same capillary using a value of  $0.00164 \text{ cm}^{-1}$  for the theoretical scattering intensity of water. To calculate the theoretical scattering curves using the program CRYSOLO (49), we used the atomic coordinates of the conformations observed in crystal forms 2 and 3, in which dummy coordinates for the missing disordered residues (see Table S2 in the supplemental material) were added manually. The agreement between our models and the experimental data were evaluated by examining the distribution of reduced residuals as a function of  $q$   $[R(q)]$ , given by the following expression:  $[I_{\text{exp}}(q) - I_{\text{calc}}(q)]/\sigma_{\text{exp}}(q)$ , where  $I_{\text{exp}}(q)$  is the experimental value of  $I$  as a function of  $q$ ,  $I_{\text{calc}}(q)$  is the

calculated value of  $I$  as a function of  $q$ , and  $\sigma_{\text{exp}}(q)$  is the experimental standard deviation as a function of  $q$ .

The splicing of the experimental curves did not interfere with the fitting of the models, while it allowed us to take advantage of the better statistical quality of the high concentration data at high  $q$  values. The SAXS data showed that pNS3h is a monomer and not the dimer present in all our crystal forms (see Results). We were not able to test the oligomeric state under the crystallization conditions listed in Table 1 to see if they induce dimerization because of the poor solubility of the protein under those conditions and the high viscosity introduced by the high concentration of high-molecular-weight polyethylene glycol.

To investigate the effect of nonhydrolyzable ATP analogs, we used ADP·BeF<sub>3</sub>, which showed a strong inhibitory effect, as did AMPPcP, on the ATPase activity of pNS3h (Fig. 1E). SAXS measurements of pNS3h in

**FIG 2** Structural comparison of NS3h orthologs. (A) Ribbon diagram of the pNS3h structure in its closed conformation from crystal form 2 (PDB accession no. 4CBG) (left), the homology model (<http://www.bioacademy.gr/bioinformatics/csfv/Welcome.html>) (second panel), HCV NS3h (PDB accession no. 1A1V) (third panel), and DENV-4 NS3h (PDB accession no. 2JLQ) (right). The proteins were superposed on D1 using the PDBFold program and are displayed in the same orientation. The three globular domains are colored green (D1), pink (D2), and blue (D3). (B) Structure-based alignment (produced using the Multalign and ESPript, version 2.2, programs) of pNS3h with its HCV and flavivirus counterparts. The CSFV (strain Alfort; GenBank accession no. J04358.2), HCV (strain H77; GenBank accession no. ACA48642), and DENV-4 (GenBank accession no. AAW30973) amino acid sequences of NS3h were retrieved from GenBank. The secondary structure elements of the CSFV, HCV, and DENV-4 NS3h proteins are displayed above the alignment. Identical or chemically similar residues are indicated at each position with a red background or red font, respectively. The residues in NS3 that allow the formation of core-less infectious pestivirus particles when substituted (described in Fig. 4) are highlighted in green. The residues deleted in the  $\Delta$ 1,  $\Delta$ 2, and  $\Delta$ 14 mutants (described in Fig. 3) are indicated by horizontal lines on top of the alignment. (C) The histograms show the percent amino acid sequence identity, the percentage of residues aligned, and the RMSD ( $\text{\AA}$ ) after the structure-based alignment between CSFV and HCV, CSFV and DENV, and HCV and DENV.





the presence of ADP·BeF<sub>3</sub> were recorded at beamline ID14-3 (ESRF) using a Pilatus 1M detector and X rays with a  $\lambda$  of 0.93 Å. The protein was in SAXS buffer with 0.4 mM MnCl<sub>2</sub> and 10 mM NaF in the presence or absence of 1 mM ADP and 1.5 mM BeCl<sub>2</sub> to make ADP·BeF<sub>3</sub> in solution (28). The data were processed as described above and confirmed that addition of just MnCl<sub>2</sub> and NaF with no ADP had no effect (see Fig. S1B in the supplemental material). To compare the resulting experimental scattering curve with the corresponding calculated curve obtained from the coordinates of the closed conformation (from crystal form 2), coordinates for the ADP·BeF<sub>3</sub> molecule were added to the pNS3h atomic model. To this end, we superposed the available X-ray structure of HCV NS3h in complex with ADP·BeF<sub>3</sub> onto that of pNS3h (superposing only on D1). Comparison of the calculated scattering curves obtained in the absence and presence of ADP·BeF<sub>3</sub> indicated a weak nucleotide contribution to the total scattering, which did not critically depend on the exact location of the nucleotide on the protein (see Fig. S1C in the supplemental material).

**Illustrations.** Figures were prepared using ESPript (50), PyMOL (<http://pymol.sourceforge.net>), and Ribbons software. The structural alignments were done using the PDBFold program from the EMBL-EBI website (<http://www.ebi.ac.uk/msd-srv/ssm/>) and the LSQMAN program (Upsala Software Factory).

**Protein structure accession numbers.** The atomic coordinates and structure factor amplitudes of pNS3h have been deposited at the Protein Data Bank (PDB) under accession numbers 4CBH (crystal form 1, wild type), 4CBG (crystal form 2, wild type), 4CBI (crystal form 3, wild type), 4CBL (N588Y mutant), and 4CBM (Q600K mutant).

## RESULTS

**Biochemical characterization of CSFV NS3.** We made recombinant constructs of CSFV full-length NS3 (residues 1 to 683 continued by the 8 N-terminal residues of NS4A; Fig. 1A) containing protease and helicase domains, and the N termini of the constructs were fused with the protease cofactor, residues 21 to 55 of NS4A, which contribute to the folded protease domain. These constructs correspond to the wild type (pNS3ph), catalytic mutants with mutation of the protease (pNS3p\*h, in which catalytic residue S163 is changed to alanine) and of the helicase (pNS3p\*h\*, in which the catalytic residue K232 of H1 or the Walker A motif is replaced by alanine), and mutants with both catalytic mutations (pNS3h\*p\*). We also made two constructs spanning the helicase domain: pNS3h1 (starting at NS3 residue 193), with its corresponding catalytic mutant being pNS3h\*1, and pNS3h2 (starting at NS3 residue 173). pNS3h1 spans the complete helicase and contains the linker connecting it to the upstream pNS3p domain. pNS3h2 has a further N-terminal extension that includes the C-terminal portion of pNS3p (33). All the constructs are listed in Fig. 1A and were expressed in *E. coli* (Fig. 1B). The ATP hydrolysis activity of the proteins, examined under steady-state conditions, showed that they follow standard Michaelis-Menten kinetics (Fig. 1C), with similar enzymatic properties being found between

full-length pNS3 and its helicase domain (Fig. 1C and D). The corresponding helicase catalytic mutants (h\*) showed no activity, as expected, when assayed under conditions identical to those used for the wild-type versions (data not shown) and served as controls. We also compared the effect of nonhydrolyzable ATP mimics on the steady-state kinetics of ATP hydrolysis of pNS3h1, using ADP·BeF<sub>3</sub>, AMPPcP, and ATPγS. Although the assay was not designed to provide a quantitative description, we found that ADP·BeF<sub>3</sub> and AMPPcP efficiently inhibited the ATPase activity, while ATPγS was much less efficient at inhibiting the ATPase activity (Fig. 1E). Comparison with the findings of similar studies using NS3h orthologs of the *Flaviviridae* family indicated that our results are similar to those obtained with the flaviviruses Murray valley encephalitis virus (MVEV) and dengue virus serotype 4 (DENV-4), for which the helicase domain and the full-length pNS3 had similar  $K_m$  values for ATP (Fig. 1F) (27, 51). However, as shown in Fig. 1F, in similar studies with HCV and DENV-2, the NS3h domain was reported to have a  $K_m$  for ATP 1 order of magnitude (or more) lower than that of the full-length NS3 (52, 53). We cannot explain the discrepancies between the different reported  $K_m$  values (especially between very closely related flaviviruses). With pNS3, however, we have reproducibly found the same results under a number of different conditions (data not shown). We also tested the RNA unwinding activity of the various pNS3 constructs using a duplex with a 14-base overhang at the 3' end of the loading strand (see Materials and Methods for details) (Fig. 1G). In this assay, constructs pNS3ph and pNS3p\*h were active, pNS3h2 displayed reduced activity, and pNS3h1 was inactive. These results show that, like in HCV and flavivirus NS3 (17, 29), the protease domain or portions of it modulate the pNS3 helicase activity. Our data thus reinforce the concept that in the *Flaviviridae* family the two functions—protease and helicase—are covalently linked in the same polypeptide chain for regulatory purposes.

**Crystallization and structure determination.** All our crystallization studies of pNS3h were done using the construct pNS3h1 (Fig. 1A). We obtained crystal forms 1 and 2 with the unsubstituted protein and the selenomethionine (SeMet)-derivatized protein, respectively. In later attempts to crystallize a complex with a nonhydrolyzable ATP analog, we obtained yet a third crystal form (crystal form 3) of apo-NS3h (i.e., it did not show evidence of a bound ATP analog). In addition, we crystallized two pNS3h mutants, N588Y and Q600K. The N588Y and Q600K mutations had been individually identified as allowing replication and propagation of core-less CSFV particles in tissue culture (24). The structures were determined and refined to a 2.5-Å resolution for the crystal with the best diffraction (crystal form 1), as described in Materials and Methods. Table 1 lists the relevant crystallographic

**FIG 4** Mapping of the mutations in NS3 that allow formation of core-independent infectious pestivirus particles. (A) Surface representation of wild-type pNS3h1 recapitulating the locations of all the mutations (in red) that have been individually shown to rescue the viability of core-less CSFV particles. (B) Crystal structure of the pNS3h N588Y mutant in surface representation and in the same orientation as the wild-type enzyme in panel A. (C) (Left) Structure of the Q600K mutant. Because residue Q600 is buried, the surface is shown semitransparently. (Right) Zoom view of the Q600K mutant (the backbone is a green C- $\alpha$  trace; side chains are yellow sticks) superposed onto wild-type pNS3h (red, C- $\alpha$  trace; white sticks, side chains) as viewed from the ATP binding site (arrows in panels A and B). In wild-type pNS3h, the Q600 side chain makes a bidentate hydrogen bond with the E651 side chain (which is protonated at neutral pH, as it displays a  $pK_a$  of 7.5). Both are represented as white sticks. In the Q600K mutant, the K600 side chain interacts in the same way with E651 (both side chains are shown as yellow sticks), but in this mutant it makes a salt bridge and compensates for the E651 negative charge (in this case, the  $pK_a$  of E651 is 5.5). As the distances between the C- $\alpha$  atoms at positions 600 and 651 remain the same, the longer K600 side chain is in a slightly strained conformation. The side chain corresponding to other mutations with the same phenotype are also indicated in wild-type pNS3h (white sticks). (D) (Left) Unwinding activity of wild-type and mutant pNS3p\*h. (Right) The bar graph represents the results of two independent RNA unwinding experiments made with two different preparations of proteins. The percentage of RNA unwound was calculated as described in the legend to Fig. 1.

statistics, and Table S2 in the supplemental material lists the disordered segments observed in the different independent molecules of the asymmetric units of the crystals.

**Overall structure.** The X-ray structure of apo-pNS3h is displayed in Fig. 2A, next to the reported homology model based on the structure of the HCV NS3 helicase (32). For comparison, the X-ray structures of NS3h from HCV and NS3h from DENV are also displayed. The corresponding structural alignment is shown in Fig. 2B, along with the secondary structure elements. pNS3h has an arrowhead shape, with its three domains, D1 (193 to 356), D2 (residues 357 to 527), and D3 (residues 528 to 683), being separated by deep clefts (Fig. 2A). The helicase signature amino acid sequence motifs present in D1 and D2 are indicated with the same color code in Fig. 2B and 5C. D3, which is less conserved, is predominantly  $\alpha$  helical. The interface between the D1-D2 RecA-like core and D3 forms a long and basic NABG running across one face of the molecule (Fig. 2A). The major interdomain contacts include helix  $\alpha 6$  in D1 packing against helices  $\alpha 9$  and  $\alpha 10$  in D3 and a long  $\beta$  hairpin ( $\beta 14$  and  $\beta 15$ ), structurally conserved across the members of the *Flaviviridae* family, that projects from D2 into D3 (Fig. 2A). D3, together with the conserved  $\beta$  hairpin, is believed to play a key role in nucleic acid unwinding by disrupting the double-stranded region of a partially duplex nucleic acid (54, 55).

D1 and D2 exhibit roughly 30 and 20% amino acid sequence similarity with their counterparts from HCV and DENV NS3 helicases, respectively (Fig. 2C), and can be individually superposed to within a root mean square deviation (RMSD) of 2 Å, with about 80% of the residues being aligned (Fig. 2C). In contrast, D3 is more distant and displays less than 10% sequence identity to its counterparts from HCV and DENV NS3 helicases (Fig. 2C). There is a common D3 core of three  $\alpha$  helices (encompassing about 20% of the aligned residues) that is shared between the three genera (shown in blue in Fig. 3A and B). This core is extended to six helices (with the addition of the yellow helices in Fig. 3A and B, amounting to 40% aligned residues) when only pestiviruses and HCV are compared (Fig. 2B and 3A). In spite of being closer to HCV, however, D3 in pNS3 is substantially different, in particular because of two important insertions (L1 and helix  $\alpha 14$ ; Fig. 2B and 3A) which were not accounted for in the recently published homology model of CSFV NS3h (32) (Fig. 2A; compare the first and second panels). The L1 loop projects into the NABG, taking up a similar spatial location as the C-terminal helix of DENV D3, which also projects within the NABG (Fig. 2A; compare the first and fourth panels). In HCV NS3, the NABG is unoccluded (Fig. 2A, third panel). Because pestivirus and DENV NS3 unwind only RNA duplexes, in contrast to HCV NS3, which can unwind RNA, DNA, and DNA/RNA hybrid double-stranded molecules, it is possible that the differences observed in NABG could account for the differences in unwinding specificity. In an attempt to test this hypothesis, we generated proteins carrying either a complete or a partial deletion of the L1 loop:  $\Delta 1$ , which contained a deletion of residues V612 to A634, and  $\Delta 2$ , which contained a deletion of residues F614 to D627. Since pNS3ph and pNS3p<sup>h</sup> exhibit similar RNA unwinding levels (Fig. 1G), we chose to introduce the mutations in the background of the latter construct to avoid possible artifacts due to the autocatalytic activity described for pNS3ph by Lamp et al. (6). Both deletion mutants were active and able to support RNA unwinding activity (Fig. 3C). However, the deletion of the L1 loop did not allow the enzyme to unwind DNA duplexes (data not shown), suggesting that additional features and

not just a more open NABG are involved. Proteins harboring a deletion of helix  $\alpha 14$  or a deletion of both helix  $\alpha 14$  and loop L1 were defective in 3D folding and were unstable (data not shown), and so we were not able to test them for DNA unwinding. In summary, our results indicate that the presence of the L1 loop is dispensable for RNA unwinding, but its absence by itself does not result in a broader unwinding specificity.

**Putative genome-packaging function.** Protein NS3 has been implicated in genome encapsidation as an RNP complex with the core protein to allow efficient budding of infectious particles. Both in HCV (20, 21, 56) and in yellow fever virus (22, 23), the NS3 mutations rescuing impaired genomic RNP formation map to D1 and D2. In contrast, the mutations that rescue infectious pestivirus particle formation in the absence of a functional core protein (24) all map to D3 (Fig. 4A). However, we observed that they do not make a clear cluster and are relatively distant from each other at the surface of the molecule (Fig. 4A). Among them, one is located by the NABG (N588Y), and another one (Q600K) is internal in the structure, introducing an internal charge (Fig. 4A). Because these mutations could affect the structure in a way that cannot be predicted, we crystallized and determined the X-ray structures of these two mutants (Fig. 4B and C). Q600 is buried in D3 (Fig. 4C, left), with its side chain making a bidentate hydrogen bond with the carboxylate group of E651, such that both side chains face each other in an extended conformation (Fig. 4C, right). In the Q600K mutant, the lysine side chain makes a salt bridge and hydrogen bond with the carboxylate group of E651, maintaining the distance between the corresponding C- $\alpha$  atoms. This involves a relatively strained rotamer of the lysine side chain, which is longer than that of glutamine (Fig. 4C, right). We used the PROPKA web interface (57) to calculate the pK<sub>a</sub> of E651. In the wild-type enzyme, the pK<sub>a</sub> is shifted to 7.5, while in the mutant it is 5.5, a value more in line with the pK<sub>a</sub> of the glutamate side chain when it is accessible to solvent. As a consequence, in spite of the introduction of a positive charge with the Q600K mutation, the overall charge does not change because E651 is not protonated like it is in the wild-type enzyme and the salt bridge with K600 compensates for its negative charge. Because this change is in the D3 interior, it does not result in any obvious new surface feature, such as a change in the surface hydrophobicity or in the surface electrostatic potential with respect to the values for the wild-type enzyme. Taken together, the structures show that the mutations do not map to a specific surface site on the pNS3 helicase that could be involved in protein/protein interactions with host partners. We also compared the RNA unwinding activity of wild-type and mutant proteins in the context of the full-length pNS3p<sup>h</sup> construct. Again, we found no significant differences (Fig. 4D), leaving open the debate for this intriguing role of NS3 in virus encapsidation.

**Conformational dynamics.** Comparison of the various independent copies of pNS3h within and across crystal forms (including the two mutants) indicated that all crystals have 4 molecules in the asymmetric unit organized in two pairs. The molecules within each pair are related by a local 2-fold axis about which D1 and D3 make a head-to-tail dimer interaction (Fig. 5A), burying from solvent a surface area of about 2,400 Å<sup>2</sup> with a surface complementarity coefficient (58) of 0.62. Within each pair, one protomer adopts a closed conformation and the other adopts an open conformation with different orientations of D2 (Fig. 5B). Although they are crystallographically independent, the two pairs found in each crystal form are very similar to each other (see Table S3A in

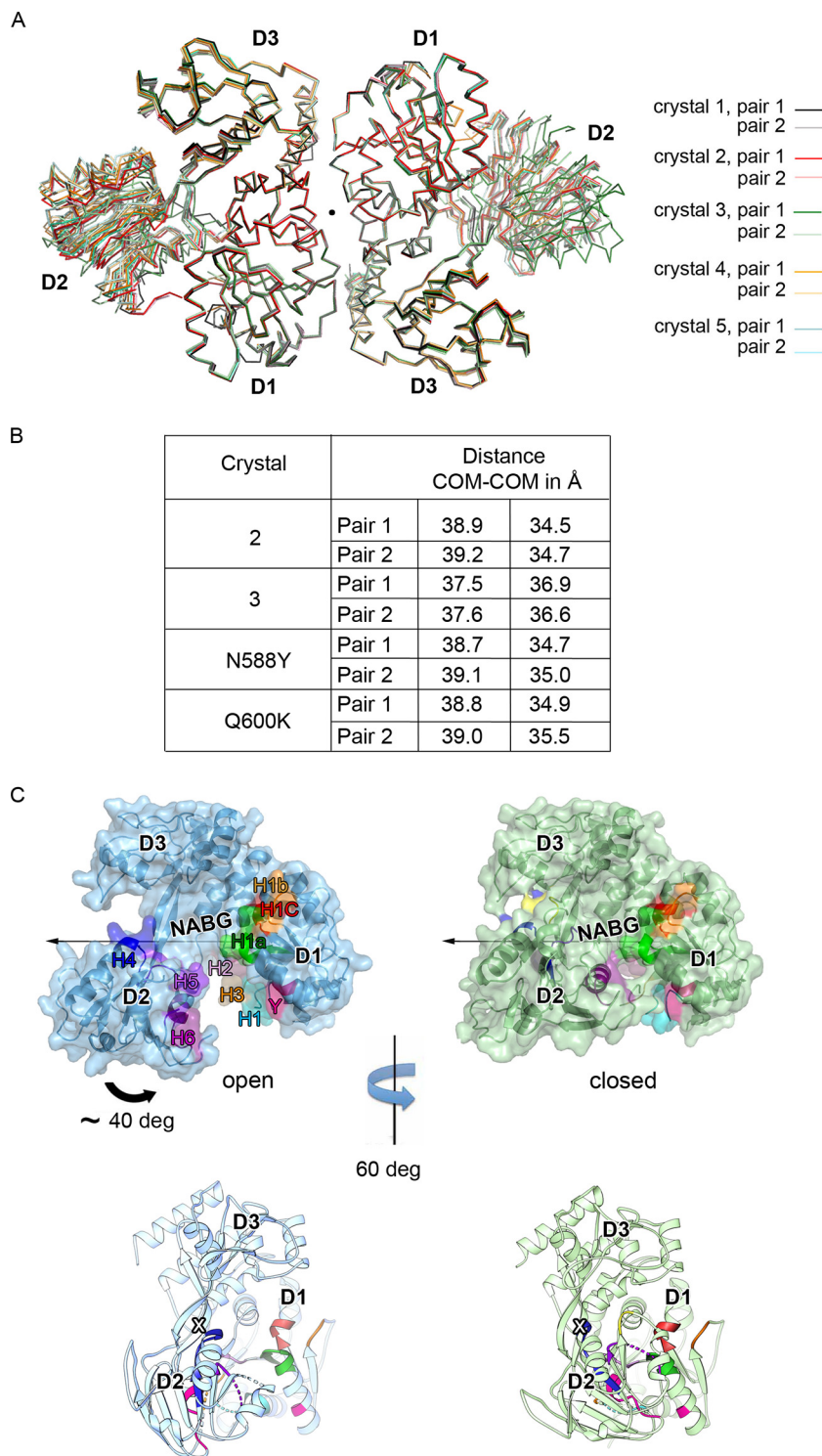
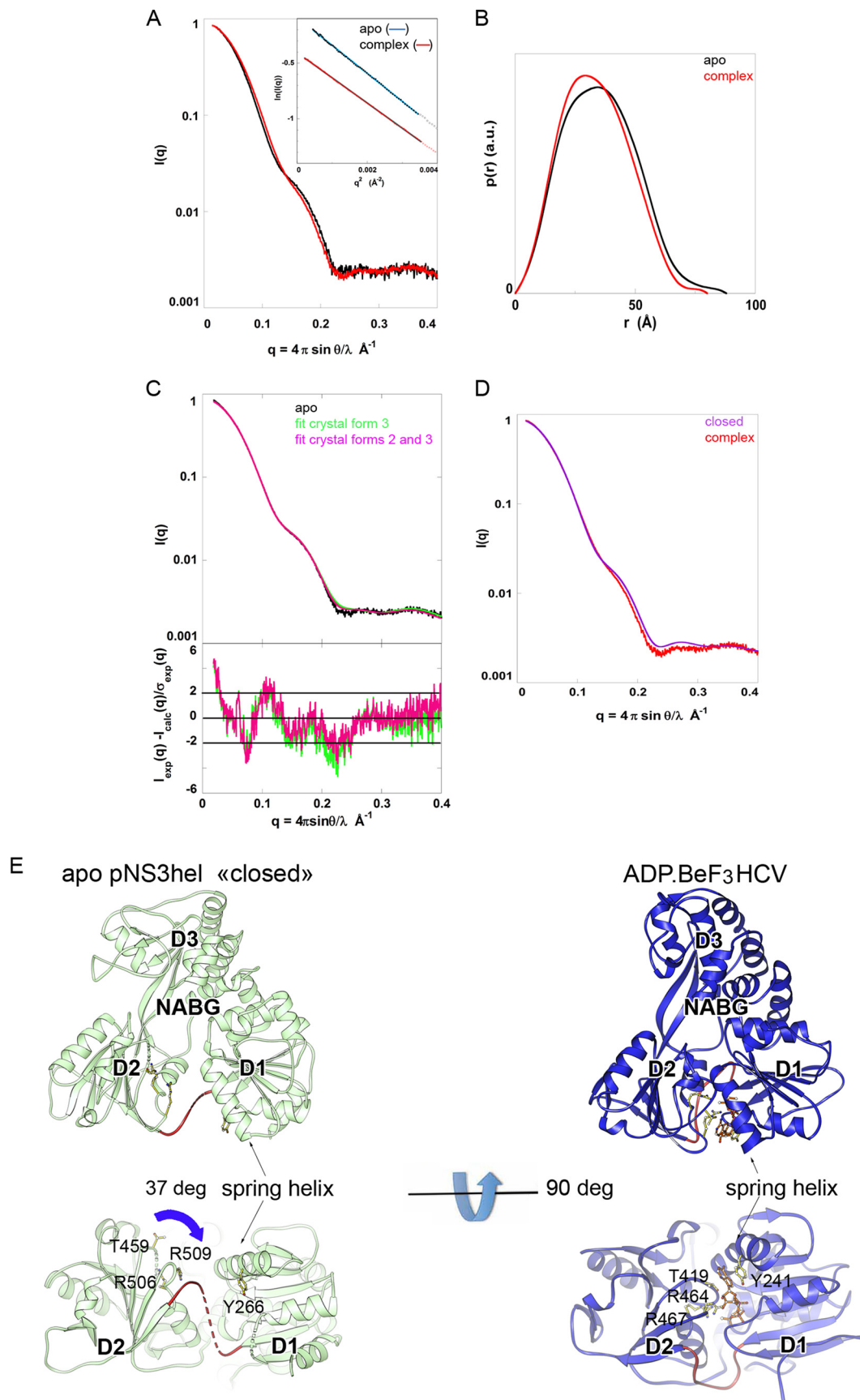


**FIG 5** pNS3h and its conformational dynamics. (A) The crystallographic dimer observed in the various pNS3h crystal forms. pNS3h molecules within the AU of the crystals are related by a local 2-fold axis about which they make head-to-tail dimer interactions. This axis is perpendicular to the plane of the figure, and its intersection with this plane is represented here by a central black dot. The plot shows the 10 independent copies of the dimers superposed on the local 2-fold axes, showing that D1 and D3 superpose well but D2 has different orientations in each case. (B) Distances between the centers of mass (COM) of D1 and D2 (measured in Å). The distances were calculated using the same number of atoms for each domain in all molecules. The two columns of data correspond to the results for the two molecules within the crystallographic dimer displayed in panel A. In total, there are 16 protomers in which D2 was ordered and for which the distances between centers of mass could be determined. (C) The two conformations in crystal form 2. (Top) pNS3h in surface representation highlighting its characteristic arrowhead shape. Crystal form 2 displays the most open (left, light blue) and closed (right, pale green) conformations of pNS3h, shown here with D1 and D3 in the same orientation. D2 rotates by about 40 degrees as a rigid body around a hinge axis tilted by roughly 30 degrees with respect to the plane of the paper (the projection on the plane of the paper of the hinge axis is drawn as a thin black arrow). (Bottom) The same molecules from the top panels viewed down the hinge axis, with an X denoting the intersection of the hinge axis with the plane of the surface. The conserved helicase motifs are colored as described in the legend to Fig. 2B: cyan (H1 or Walker A), green (H1a), orange (H1b), red (H1c), pink (H2 or Walker B), light orange (H3), blue (H4), yellow (H4a), light purple (H5), and purple (H6). Motif Y, present only in the pesti- and hepacivirus genera, is shown in dark pink.







the supplemental material). The head-to-tail dimer was present in all crystal forms, including form 1, which displayed no electron density for D2. In the other forms, D2 deviates from the local 2-fold axis, with dimers of D1-D3 superposing with an RMSD of under 0.6 Å in all the structures, whereas inclusion of D2 brings the RMSD values between dimers to about 3 Å (see Table S3A in the supplemental material). The individual D2 domains superpose separately with an RMSD of about 0.4 Å, indicating that this domain moves as a rigid body (see Table S4 in the supplemental material).

Each D2 conformation is stabilized by specific crystal-packing interactions. The crystals of the N588Y and Q600Y mutants are very similar to crystal form 2, differing essentially in the *b* axis by about 10 Å (Table 1). Correspondingly, the individual open and closed conformations of pNS3h observed in these crystals are very similar to each other. The transformation from open to closed corresponds to a roughly 40-degree rotation of D2 (Fig. 5C) about an axis tilted 30 degrees with respect to the plane of the figure. In crystal form 3, D2 adopts an intermediate orientation between the two extreme conformations of crystal form 2 (Fig. 5B; see also Table S3A in the supplemental material). We used normal modes analysis (NMA) to study the conformational change, taking the most open and closed conformations of crystal form 2 (Fig. 5C) as references (see Materials and Methods). The results showed that the two lowest-frequency modes account for 90% of the observed open-to-closed transition (see Movie S1 in the supplemental material). Applying the transformation corresponding to these two harmonic modes to the open form yielded a closed form with an RMSD of 1.1 Å with respect to the observed closed form (compared to an RMSD of roughly 5 Å between the experimentally observed open and closed forms; see Table S3B in the supplemental material). We also found that the two intermediate conformations (Fig. 5B) observed in crystal form 3 were within the path predicted by NMA (data not shown).

**Conformation in solution.** The SAXS analysis of pNS3h (always using the pNS3h1 construct; Fig. 1A) in solution (Fig. 6A to D) revealed a Guinier plot corresponding to a radius of gyration ( $R_g$ ) of  $27.5 \pm 0.3$  Å and an estimated molecular mass of 57.5 kDa, in agreement with the value calculated from the amino acid sequence, 55.9 kDa (Fig. 6A, inset). This indicates that in spite of the large surface area buried in the dimer observed in the crystals (Fig. 5A), pNS3h dimerizes only under the particular crystallization conditions used (listed in Table 1) and not under more physiological conditions, such as those used in the SAXS experiments (20 mM Tris-HCl, pH 7.5, 100 mM NaCl, 2 mM DTT). We also confirmed the monomeric conformation of pNS3h in solution by analytical ultracentrifugation (data not shown). The pair distance distribution function [ $p(r)$ ] (Fig. 6B) calculated from the scatter-

ing curve (Fig. 6A) yielded a maximum intramolecular distance ( $D_{\max}$ ) of 88 Å and an accompanying  $R_g$  value of 27.2 Å (Fig. 6B, black curve), very close to the values obtained by the Guinier determination indicated above.

We compared the experimental scattering pattern with the curve calculated from the atomic coordinates of pNS3h from the various structures (both by visual inspection and by the chi-square test). The conformations observed in crystal form 3, which are intermediate between the open and closed conformations of crystal form 2 (Fig. 5B), fit much better ( $\chi^2 = 2.4$ ) than the individual open ( $\chi^2 = 28.0$ ) and closed ( $\chi^2 = 29.5$ ) conformations of crystal form 2 (see Fig. S1D in the supplemental material). We obtained the best fit ( $\chi^2 = 2.0$ ) by using a linear combination of three forms, open, closed (from crystal form 2), plus either conformation of crystal form 3 (Fig. 6C). However, the increase in the number of degrees of freedom by adding more models may artificially improve the match between calculated and experimental curves, so these data must be interpreted cautiously.

The most conspicuous variation among the calculated curves occurred in the region of the shoulder around a  $q$  value of  $0.16 \text{ Å}^{-1}$  (see Fig. S1D in the supplemental material), which corresponds to about 40 Å. This is roughly the distance between the centers of mass of D1 and D2 (Fig. 5B), suggesting that the variation is due to the interdomain vectors. So, the shoulder in the scattering curve appears to report about the position of D2.

The scattering from a solution containing a mixture of conformations is the average of all scattering curves weighted by the respective fractional concentration of each conformation. SAXS cannot unambiguously discriminate between an ensemble of conformations in solution and a single conformation whose scattering curve is identical to the experimental average. In the case of small amplitude differences, as observed here, such a conformation would be close to the centroid of the ensemble. This is also the case for the conformations found in crystal form 3, in which D2 is about midway between the two more extreme conformations (Fig. 5B). The better agreement with the experimental SAXS data of the scattering curves calculated from these intermediate conformations may thus be fortuitous, in particular since D2 is maintained in this intermediate conformation essentially through crystal-packing contacts. Another sign of its high mobility is that in crystal form 3 D2 displays mean B factors that are significantly higher than those of the other domains (see Table S5 in the supplemental material) and displays very poor electron density in the two open conformations of this crystal form.

**Nucleotide binding.** Structural studies of HCV NS3 have shown that binding of a nonhydrolyzable ATP analog, such as ADP·BeF<sub>3</sub>, results in a closed conformation of the molecule that is

**FIG 6** SAXS analysis. (A and B) Experimental scattering curves (A) and  $p(r)$  (B) of pNS3h in the apo-form (black curves) and in complex with ADP·BeF<sub>3</sub> (red curves). (Inset in panel A) Guinier plots of the two samples. The regression lines are shown as cyan and gray, while the data used for the fit are indicated as black and red dots, respectively. The  $y$  axis of one data set was shifted vertically for clarity. a.u., arbitrary units. (C) The linear combination of the scattering curves derived from the conformations observed in crystal forms 2 and 3 together (magenta,  $\chi^2 = 2.0$ ) fits the experimental scattering curve from apo-pNS3h (black) slightly better than the calculated scattering curve obtained with either of the intermediate forms of crystal form 3 (green,  $\chi^2 = 2.4$ ), as indicated by the reduction of the corresponding residuals (bottom). (D) Experimental scattering curve of pNS3h in complex with ADP·BeF<sub>3</sub> (red) superposed on the calculated scattering curve from the most closed conformation observed in crystal form 2 (purple), showing that the complex has a more compact conformation. (E) The remaining rearrangement necessary to generate the nucleotide-binding site in pNS3h. (Left) Apo-pNS3h in its closed conformation (pale green); (right) HCV NS3h in complex with ADP·BeF<sub>3</sub> (PDB accession no. 3O8D) (blue). The structures were superposed on D1 and D3 using PDBfold. The D1-D2 linker is colored red in both structures. Dashed lines indicate disordered residues in the pNS3h structure. ADP·BeF<sub>3</sub> and residues interacting with it in HCV NS3h are shown as orange and yellow sticks, respectively. The equivalent residues in pNS3h are also displayed in the same way, to show that a rotation of D2 of about 37 degrees (blue arrow) would be necessary to bring R506 and R509 into superposition with their HCV counterparts that bind the nucleotide, while displacing the D1-D2 linker out of the way.

different from the conformation of the available apo-forms (28, 59). Although our attempts to crystallize a similar complex with pNS3h failed, we observed that its X-ray-scattering pattern in solution was clearly different in the presence of ADP·BeF<sub>3</sub> (Fig. 6). The observed differences are best visualized when comparing the  $p(r)$  profiles (Fig. 6B). The presence of ADP·BeF<sub>3</sub> results in an  $R_g$  reduced by 1 Å and a  $D_{max}$  reduced by about 8 Å as the  $p(r)$  profile becomes distinctly narrower, with its right-hand side shifting leftward by about 3 Å. These observations suggest that pNS3h becomes more compact when in complex with ADP·BeF<sub>3</sub> (Fig. 6A and B). To confirm this, we compared the experimental SAXS curve with the one calculated with the coordinates of the closed form (complemented by modeling an ADP·BeF<sub>3</sub> molecule guided by the structure of the HCV NS3h complex). The results indicate that the nucleotide-bound conformation is different and more compact than the most closed apo-form found in our crystals (Fig. 6D).

Structural studies of HCV and DENV NS3h have shown that the incoming nucleotide binds at the interface between D1 and D2 through residues of motifs H1, H2, and H3 in D1 and H5 and H6 in D2 (28, 60). The structure of the closed apo-pNS3h conformation has the D1-D2 linker intercalated between these motifs (Fig. 6E). Comparison with HCV NS3h in complex with ADP·BeF<sub>3</sub> suggests that the side chains of Tyr 266 and Thr 459 in pNS3h would sandwich the ADP adenine base from the nonhydrolyzable ATP analog, playing the same role as Tyr 242 and Thr 419 in HCV NS3h (28). However, in order to reach such a conformation, a rotation of D2 of about 37 degrees from its location in the apo-pNS3h conformation is necessary (indicated by the blue arrow in Fig. 6E, lower left). Such a rotation would simultaneously displace the D1-D2 linker to a location similar to that of its counterpart in HCV NS3h (Fig. 6, lower right), resulting in a more compact form, in line with the findings of SAXS analyses.

## DISCUSSION

In this work, we structurally and functionally characterized the pestivirus NS3 helicase domain. In isolation, the pNS3h domain efficiently hydrolyzes ATP but is not active in unwinding duplex RNA, in contrast to full-length pNS3 or an N-terminally extended version of pNS3h that includes parts of the protease domain, which actively unwound RNA in our assays. Modulation of the helicase activity by the protease domain or by parts of it has already been described for flaviviruses and for HCV NS3 (17, 29). As proposed for DENV-4, the presence of basic residues in the protease domain could facilitate the diffusion of ATP toward the nucleotide binding site, optimizing its hydrolysis rate (61). Indeed, our ATPase assay showed that despite having similar affinities for ATP, full-length pNS3 and the pNS3h2 construct have a  $k_{cat}$  value that is twice that of pNS3h1, indicating that they hydrolyze ATP more efficiently and suggesting that a certain threshold in the rate of ATP hydrolysis may be necessary for the unwinding activity. The conserved modulation of the helicase activity by the protease domain across the *Flaviviridae* family suggests that this domain may play a regulatory role during virus replication. The recently reported autocatalytic proteolysis between the protease and helicase domains (6) may represent a way to control helicase activity during infection. Indeed, this natural cleavage results in two forms, one beginning at M193 (corresponding to our pNS3h1 construct) and the other beginning at K160, i.e., a form longer than the pNS3h2 construct (Fig. 1), which has intermediate unwinding activity.

The nucleic acid unwinding mechanism of NS3 is not yet understood, in part because it is not clear what motifs are involved in separating the two strands of the nucleic acid duplex. The crystal structure of the DNA helicase Hel308 from *Archaeoglobus fulgidus* in complex with a partially unwound DNA duplex provided important structural insight about its unwinding mechanism (54). Extrapolation from this work would suggest that both the  $\beta$  hairpin and the D2-D3 interface are key players for nucleic acid unwinding in pNS3h. Indeed, the  $\beta$  hairpin was shown to be important for the helicase activity of HCV NS3 (62). Functionally, the pestivirus helicase domain resembles the flavivirus NS3 helicase more than it resembles the HCV counterpart, since both pestivirus and flaviviruses exclusively unwind RNA duplexes, whereas HCV NS3h also unwinds DNA and DNA/RNA hybrid double-stranded nucleic acids. Although pNS3 and the HCV NS3 are structurally closer to each other than to flavivirus NS3 (Fig. 2 and 3), the two insertions in D3—the L1 loop and helix  $\alpha$ 14—partially occlude the NABG, as does the C-terminal helix  $\alpha$ 12 of DENV NS3h, while in HCV NS3h the NABG is unoccluded. Deletion of the L1 loop showed that it is not required for RNA unwinding activity but did not allow a gain of function, i.e., to unwind DNA duplexes. With regard to this RNA-only specificity, the DENV NS3h residues that make specific contact with the 2' OH moieties of the bound single-stranded RNA (ssRNA) (60) are conserved in both pNS3h and HCV NS3h (see Table S6 in the supplemental material), but in the latter they do not make specific 2' OH interactions (59). Thus, the predictions of the pNS3h residues that may specifically contact the 2' OH moiety are inconclusive.

The NS3 helicase domain has also been implicated in virus morphogenesis, although the mechanism behind it remains unknown. In this work, we mapped the mutations conferring viability to core-less pestivirus particles to D3, but we observed that they do not make any obvious surface patch that could be interpreted as the binding site for a protein or other molecular partner and do not change the surface hydrophobicity or the electrostatic potential with respect to the values for the wild-type enzyme. Also, they do not change the *in vitro* capacity of pNS3 to unwind RNA (Fig. 4), suggesting that, similar to yellow fever virus (23), the NS3 role during virus assembly is independent of its enzymatic functions. These structural and functional data, although negative, could steer future efforts toward the elucidation of this intriguing role of NS3 in the *Flaviviridae* family during the virus cycle.

Our data suggest that pNS3h does not adopt a unique, well-defined apo-conformation in solution but explores a dynamic ensemble of conformations sampled by the various crystal forms. Because it is about midway between the open and closed forms, the intermediate conformations observed in crystal form 3 appear to be close to the experimental average of the ensemble of conformations sampled by the molecule in solution, explaining the better agreement between the scattering pattern calculated from these forms and the experimental SAXS curve. Binding of a nonhydrolyzable ATP analog stabilizes the protein in a different conformation that is more compact than the closed apo-form identified in our crystals. Structures displaying similar closed and open conformations of the apo-NS3 enzyme from HCV have also been reported, albeit from NS3 belonging to different HCV genotypes (25, 63–65). Recent molecular dynamics simulations indicated that DENV apo-NS3h also appears to oscillate between open and closed conformations (66), again suggesting an intrinsically dynamic behavior, although the structures of the apo-form of the

enzyme in different conformations are not available. SAXS analyses of HCV and flavivirus NS3h in the presence or absence of an ATP analog might provide useful comparative information.

In conclusion, our data fill a gap by providing the structure of the pestivirus helicase, which could not have been accurately predicted by homology modeling on the basis of its orthologs of known structure. Our results also support the idea that the unwinding and translocation functions of NS3 require a highly dynamic interplay between alternative conformations, with limited structural transitions being essential for function. This flexibility could therefore constitute a valuable target to block the replication cycle of these viruses by using antiviral compounds that stabilize the molecule in a single conformation, thereby interfering with its unwinding activity. Recent approaches designed to act allosterically to target motion in motor proteins (67) might finally result in specific inhibitors of the NS3 helicase function, which have remained elusive, in spite of intensive efforts targeting HCV NS3.

## ACKNOWLEDGMENTS

J.K. was awarded an internship from the L'Oreal Scholarship for Research for performing part of this work at the Institut Pasteur, Paris, France.

We are grateful to A. Haouz (Plate-Forme de Cristallographie, Pasteur Institute) for help with crystallization trials, Bertrand Raynal (Plate-Forme de Biophysique des Macromolécules, Pasteur Institute) for expertise in analytical ultracentrifugation, Christine Girard-Blanc (Plate-Forme, de Protéines Recombinantes en Cellules Eucaryotes, Pasteur Institute) for assistance with protein purifications, and Marie-Christine Vaney for her expert help during data collection. We thank Pablo Guardado-Calvo and Alexander Rouvinski for helpful discussions and Evelyne Richet and Raphael Laurenceau for help setting up the ATPase assay. We also thank the SLS, ESRF, and Soleil synchrotron staff for providing access to synchrotron facilities and L. Zerrad and P. Pernot for help with measurements at ID14-3 (ESRF, Grenoble, France).

## REFERENCES

- Rossi S, Toigo C, Hars J, Pol F, Hamann JL, Depner K, Le Potier MF. 2011. New insights on the management of wildlife diseases using multi-state recapture models: the case of classical swine fever in wild boar. *PLoS One* 6:e24257. <http://dx.doi.org/10.1371/journal.pone.0024257>.
- Lindenbach BM, Murray CL, Thiel HJ, Rice CM. 2013. Flaviviridae, p 712–746. Knipe DM, Howley PM, Cohen JI, Griffin DE, Lamb RA, Martin MA, Racaniello VR, Roizman B (ed), *Fields virology*, 6th ed. Lippincott Williams & Wilkins, Philadelphia, PA.
- Burbelo PD, Dubovi EJ, Simmonds P, Medina JL, Henriquez JA, Mishra N, Wagner J, Tokarz R, Cullen JM, Iadarola MJ, Rice CM, Lipkin WI, Kapoor A. 2012. Serology-enabled discovery of genetically diverse hepaciviruses in a new host. *J Virol* 86:6171–6178. <http://dx.doi.org/10.1128/JVI.00250-12>.
- Kapoor A, Simmonds P, Cullen JM, Scheel TK, Medina JL, Giannitti F, Nishiuchi E, Brock KV, Burbelo PD, Rice CM, Lipkin WI. 2013. Identification of a pegivirus (GB virus-like virus) that infects horses. *J Virol* 87:7185–7190. <http://dx.doi.org/10.1128/JVI.00324-13>.
- Lamp B, Riedel C, Roman-Sosa G, Heimann M, Jacobi S, Becher P, Thiel HJ, Rumenapf T. 2011. Biosynthesis of classical swine fever virus nonstructural proteins. *J Virol* 85:3607–3620. <http://dx.doi.org/10.1128/JVI.02206-10>.
- Lamp B, Riedel C, Wentz E, Tortorici MA, Rumenapf T. 2013. Auto-catalytic cleavage within classical swine fever virus NS3 leads to a functional separation of protease and helicase. *J Virol* 87:11872–11883. <http://dx.doi.org/10.1128/JVI.00754-13>.
- Choi KH, Groarke JM, Young DC, Kuhn RJ, Smith JL, Pevear DC, Rossmann MG. 2004. The structure of the RNA-dependent RNA polymerase from bovine viral diarrhea virus establishes the role of GTP in de novo initiation. *Proc Natl Acad Sci U S A* 101:4425–4430. <http://dx.doi.org/10.1073/pnas.0400660101>.
- Krey T, Bontems F, Vonnrhein C, Vaney MC, Bricogne G, Rumenapf T, Rey FA. 2012. Crystal structure of the pestivirus envelope glycoprotein E(rns) and mechanistic analysis of its ribonuclease activity. *Structure* 20:862–873. <http://dx.doi.org/10.1016/j.str.2012.03.018>.
- El Omari K, Iourin O, Harlos K, Grimes JM, Stuart DI. 2013. Structure of a pestivirus envelope glycoprotein E2 clarifies its role in cell entry. *Cell Rep* 3:30–35. <http://dx.doi.org/10.1016/j.celrep.2012.12.001>.
- Li Y, Wang J, Kanai R, Modis Y. 2013. Crystal structure of glycoprotein E2 from bovine viral diarrhea virus. *Proc Natl Acad Sci U S A* 110:6805–6810. <http://dx.doi.org/10.1073/pnas.1300524110>.
- Gottipati K, Ruggli N, Gerber M, Tratschin JD, Benning M, Bellamy H, Choi KH. 2013. The structure of classical swine fever virus N(pro): a novel cysteine autoprotease and zinc-binding protein involved in subversion of type I interferon induction. *PLoS Pathog* 9:e1003704. <http://dx.doi.org/10.1371/journal.ppat.1003704>.
- Zogg T, Sponring M, Schindler S, Koll M, Schneider R, Brandstetter H, Auer B. 2013. Crystal structures of the viral protease N<sup>pro</sup> imply distinct roles for the catalytic water in catalysis. *Structure* 21:929–938. <http://dx.doi.org/10.1016/j.str.2013.04.003>.
- Singleton MR, Dillingham MS, Wigley DB. 2007. Structure and mechanism of helicases and nucleic acid translocases. *Annu Rev Biochem* 76:23–50. <http://dx.doi.org/10.1146/annurev.biochem.76.052305.115300>.
- Wang CC, Huang ZS, Chiang PL, Chen CT, Wu HN. 2009. Analysis of the nucleoside triphosphatase, RNA triphosphatase, and unwinding activities of the helicase domain of dengue virus NS3 protein. *FEBS Lett* 583:691–696. <http://dx.doi.org/10.1016/j.febslet.2009.01.008>.
- Warrener P, Collett MS. 1995. Pestivirus NS3 (p80) protein possesses RNA helicase activity. *J Virol* 69:1720–1726.
- Beran RK, Pyle AM. 2008. Hepatitis C viral NS3-4A protease activity is enhanced by the NS3 helicase. *J Biol Chem* 283:29929–29937. <http://dx.doi.org/10.1074/jbc.M804065200>.
- Beran RK, Serebrov V, Pyle AM. 2007. The serine protease domain of hepatitis C viral NS3 activates RNA helicase activity by promoting the binding of RNA substrate. *J Biol Chem* 282:34913–34920. <http://dx.doi.org/10.1074/jbc.M707165200>.
- Raney KD, Sharma SD, Moustafa IM, Cameron CE. 2010. Hepatitis C virus non-structural protein 3 (HCV NS3): a multifunctional antiviral target. *J Biol Chem* 285:22725–22731. <http://dx.doi.org/10.1074/jbc.R110.125294>.
- Heaton NS, Perera R, Berger KL, Khadka S, Lacount DJ, Kuhn RJ, Randall G. 2010. Dengue virus nonstructural protein 3 redistributes fatty acid synthase to sites of viral replication and increases cellular fatty acid synthesis. *Proc Natl Acad Sci U S A* 107:17345–17350. <http://dx.doi.org/10.1073/pnas.1010811107>.
- Jones DM, Atoom AM, Zhang X, Kottitil S, Russell RS. 2011. A genetic interaction between the core and NS3 proteins of hepatitis C virus is essential for production of infectious virus. *J Virol* 85:12351–12361. <http://dx.doi.org/10.1128/JVI.05313-11>.
- Ma Y, Yates J, Liang Y, Lemon SM, Yi M. 2008. NS3 helicase domains involved in infectious intracellular hepatitis C virus particle assembly. *J Virol* 82:7624–7639. <http://dx.doi.org/10.1128/JVI.00724-08>.
- Kummerer BM, Rice CM. 2002. Mutations in the yellow fever virus nonstructural protein NS2A selectively block production of infectious particles. *J Virol* 76:4773–4784. <http://dx.doi.org/10.1128/JVI.76.10.4773-4784.2002>.
- Patkar CG, Kuhn RJ. 2008. Yellow fever virus NS3 plays an essential role in virus assembly independent of its known enzymatic functions. *J Virol* 82:3342–3352. <http://dx.doi.org/10.1128/JVI.02447-07>.
- Riedel C, Lamp B, Heimann M, König M, Blome S, Moennig V, Schuttler C, Thiel HJ, Rumenapf T. 2012. The core protein of classical swine fever virus is dispensable for virus propagation in vitro. *PLoS Pathog* 8:e1002598. <http://dx.doi.org/10.1371/journal.ppat.1002598>.
- Yao N, Hesson T, Cable M, Hong Z, Kwong AD, Le HV, Weber PC. 1997. Structure of the hepatitis C virus RNA helicase domain. *Nat Struct Biol* 4:463–467. <http://dx.doi.org/10.1038/nsb0697-463>.
- Yao N, Reichert P, Taremi SS, Prossie WW, Weber PC. 1999. Molecular views of viral polyprotein processing revealed by the crystal structure of the hepatitis C virus bifunctional protease-helicase. *Structure* 7:1353–1363. [http://dx.doi.org/10.1016/S0969-2126\(00\)80025-8](http://dx.doi.org/10.1016/S0969-2126(00)80025-8).
- Assenberg R, Mastrangelo E, Walter TS, Verma A, Milani M, Owens RJ, Stuart DI, Grimes JM, Mancini EJ. 2009. Crystal structure of a novel conformational state of the flavivirus NS3 protein: implications for polyprotein processing and viral replication. *J Virol* 83:12895–12906. <http://dx.doi.org/10.1128/JVI.00942-09>.
- Gu M, Rice CM. 2010. Three conformational snapshots of the hepatitis C



- virus NS3 helicase reveal a ratchet translocation mechanism. *Proc Natl Acad Sci U S A* 107:521–528. <http://dx.doi.org/10.1073/pnas.0913380107>.
29. Mastrangelo E, Milani M, Bollati M, Selisko B, Peyrane F, Pandini V, Sorrentino G, Canard B, Konarev PV, Svergun DI, de Lamballerie X, Coutard B, Khromykh AA, Bolognesi M. 2007. Crystal structure and activity of Kunjin virus NS3 helicase; protease and helicase domain assembly in the full length NS3 protein. *J Mol Biol* 372:444–455. <http://dx.doi.org/10.1016/j.jmb.2007.06.055>.
  30. Yamashita T, Unno H, Mori Y, Tani H, Moriishi K, Takamizawa A, Agoh M, Tsukihara T, Matsuura Y. 2008. Crystal structure of the catalytic domain of Japanese encephalitis virus NS3 helicase/nucleoside triphosphatase at a resolution of 1.8 Å. *Virology* 373:426–436. <http://dx.doi.org/10.1016/j.virol.2007.12.018>.
  31. Wen G, Chen C, Luo X, Wang Y, Zhang C, Pan Z. 2007. Identification and characterization of the NTPase activity of classical swine fever virus (CSFV) nonstructural protein 3 (NS3) expressed in bacteria. *Arch Virol* 152:1565–1573. <http://dx.doi.org/10.1007/s00705-007-0969-2>.
  32. Vlachakis D, Kossida S. 2013. Molecular modeling and pharmacophore elucidation study of the classical swine fever virus helicase as a promising pharmacological target. *PeerJ* 1:e85. <http://dx.doi.org/10.7717/peerj.85>.
  33. Wen G, Xue J, Shen Y, Zhang C, Pan Z. 2009. Characterization of classical swine fever virus (CSFV) nonstructural protein 3 (NS3) helicase activity and its modulation by CSFV RNA-dependent RNA polymerase. *Virus Res* 141:63–70. <http://dx.doi.org/10.1016/j.virusres.2008.12.014>.
  34. Broennimann C, Eikenberry EF, Henrich B, Horisberger R, Huelsen G, Pohl E, Schmitt B, Schulze-Briese C, Suzuki M, Tomizaki T, Toyokawa H, Wagner A. 2006. The PILATUS IM detector. *J Synchrotron Radiat* 13:120–130. <http://dx.doi.org/10.1107/S0909049505038665>.
  35. Kraft P, Bergamaschi A, Broennimann C, Dinapoli R, Eikenberry EF, Henrich B, Johnson I, Mozzanica A, Schlepütz CM, Willmott PR, Schmitt B. 2009. Performance of single-photon-counting PILATUS detector modules. *J Synchrotron Radiat* 16:368–375. <http://dx.doi.org/10.1107/S0909049509009911>.
  36. Kabsch W. 2010. XDS. *Acta Crystallogr D Biol Crystallogr* 66:125–132. <http://dx.doi.org/10.1107/S0907444909047337>.
  37. Evans P. 2006. Scaling and assessment of data quality. *Acta Crystallogr D Biol Crystallogr* 62:72–82. <http://dx.doi.org/10.1107/S0907444905036693>.
  38. Cowtan K. 2006. The Buccaneer software for automated model building. 1. Tracing protein chains. *Acta Crystallogr D Biol Crystallogr* 62:1002–1011. <http://dx.doi.org/10.1107/S0907444906022116>.
  39. Cowtan K. 1994. 'DM': an automated procedure for phase improvement by density modification. *Joint CCP4 ESF-EACBM Newsl Protein Crystallogr* 31:34–38.
  40. Emsley P, Lohkamp B, Scott WG, Cowtan K. 2010. Features and development of Coot. *Acta Crystallogr D Biol Crystallogr* 66:486–501. <http://dx.doi.org/10.1107/S0907444910007493>.
  41. Blanc E, Roversi P, Vonnheim C, Flensburg C, Lea SM, Bricogne G. 2004. Refinement of severely incomplete structures with maximum likelihood in BUSTER-TNT. *Acta Crystallogr D Biol Crystallogr* 60:2210–2221. <http://dx.doi.org/10.1107/S0907444904016427>.
  42. Navaza J. 1994. AMoRe: an automated package for molecular replacement. *Acta Crystallogr A Found Crystallogr* 50:157–163. <http://dx.doi.org/10.1107/S0108767393007597>.
  43. Lindahl E, Azuara C, Koehl P, Delarue M. 2006. NOMAD-Ref: visualization, deformation and refinement of macromolecular structures based on all-atom normal mode analysis. *Nucleic Acids Res* 34:W52–W56. <http://dx.doi.org/10.1093/nar/gkl082>.
  44. Suhre K, Sanejouand YH. 2004. ElNemo: a normal mode web server for protein movement analysis and the generation of templates for molecular replacement. *Nucleic Acids Res* 32:W610–W614. <http://dx.doi.org/10.1093/nar/gkh368>.
  45. David G, Pérez J. 2009. Combined sampler robot and high-performance liquid chromatography: a fully automated system for biological small-angle X-ray scattering experiments at the Synchrotron SOLEIL SWING beamline. *J Appl Crystallogr* 42:892–900. <http://dx.doi.org/10.1107/S0021889809029288>.
  46. Konarev PV, Volkov VV, Sokolova AV, Koch MHJ, Svergun DI. 2003. PRIMUS: a Windows PC-based system for small-angle scattering data analysis. *J Appl Crystallogr* 36:1277–1282. <http://dx.doi.org/10.1107/S0021889803012779>.
  47. Guinier A, Fournet G. 1955. Small angle scattering of X-rays. John Wiley & Sons, Inc, New York, NY.
  48. Svergun DI. 1992. Determination of the regularization parameter in indirect-transform methods using perceptual criteria. *J Appl Crystallogr* 25:495–503. <http://dx.doi.org/10.1107/S0021889892001663>.
  49. Svergun DI, Barberato C, Koch MHJ. 1995. CRYSOLO—a program to evaluate X-ray solution scattering of biological macromolecules from atomic coordinates. *J Appl Crystallogr* 28:768–773. <http://dx.doi.org/10.1107/S0021889895007047>.
  50. Robert X, Gouet P. 2014. Deciphering key features in protein structures with the new ENDscript server. *Nucleic Acids Res* 42:W320–W324. <http://dx.doi.org/10.1093/nar/gku316>.
  51. Luo D, Wei N, Doan DN, Paradkar PN, Chong Y, Davidson AD, Kotaka M, Lescar J, Vasudevan SG. 2010. Flexibility between the protease and helicase domains of the dengue virus NS3 protein conferred by the linker region and its functional implications. *J Biol Chem* 285:18817–18827. <http://dx.doi.org/10.1074/jbc.M109.090936>.
  52. Lam AM, Rypma RS, Frick DN. 2004. Enhanced nucleic acid binding to ATP-bound hepatitis C virus NS3 helicase at low pH activates RNA unwinding. *Nucleic Acids Res* 32:4060–4070. <http://dx.doi.org/10.1093/nar/gkh743>.
  53. Xu T, Sampath A, Chao A, Wen D, Nanao M, Chene P, Vasudevan SG, Lescar J. 2005. Structure of the dengue virus helicase/nucleoside triphosphatase catalytic domain at a resolution of 2.4 Å. *J Virol* 79:10278–10288. <http://dx.doi.org/10.1128/JVI.79.16.10278-10288.2005>.
  54. Buttner K, Nehring S, Hopfner KP. 2007. Structural basis for DNA duplex separation by a superfamily-2 helicase. *Nat Struct Mol Biol* 14:647–652. <http://dx.doi.org/10.1038/nsmb1246>.
  55. Jiang F, Ramanathan A, Miller MT, Tang GQ, Gale M, Jr, Patel SS, Marcotrigiano J. 2011. Structural basis of RNA recognition and activation by innate immune receptor RIG-I. *Nature* 479:423–427. <http://dx.doi.org/10.1038/nature10537>.
  56. Yi M, Ma Y, Yates J, Lemon SM. 2007. Compensatory mutations in E1, p7, NS2, and NS3 enhance yields of cell culture-infectious intergenotypic chimeric hepatitis C virus. *J Virol* 81:629–638. <http://dx.doi.org/10.1128/JVI.01890-06>.
  57. Rostkowski M, Olsson MH, Sondergaard CR, Jensen JH. 2011. Graphical analysis of pH-dependent properties of proteins predicted using PROPKA. *BMC Struct Biol* 11:6. <http://dx.doi.org/10.1186/1472-6807-11-6>.
  58. Lawrence MC, Colman PM. 1993. Shape complementarity at protein/protein interfaces. *J Mol Biol* 234:946–950. <http://dx.doi.org/10.1006/jmbi.1993.1648>.
  59. Appleby TC, Anderson R, Fedorova O, Pyle AM, Wang R, Liu X, Brendza KM, Somoza JR. 2011. Visualizing ATP-dependent RNA translocation by the NS3 helicase from HCV. *J Mol Biol* 405:1139–1153. <http://dx.doi.org/10.1016/j.jmb.2010.11.034>.
  60. Luo D, Xu T, Watson RP, Scherer-Becker D, Sampath A, Jahnke W, Yeong SS, Wang CH, Lim SP, Strongin A, Vasudevan SG, Lescar J. 2008. Insights into RNA unwinding and ATP hydrolysis by the flavivirus NS3 protein. *EMBO J* 27:3209–3219. <http://dx.doi.org/10.1038/emboj.2008.232>.
  61. Luo D, Xu T, Hunke C, Gruber G, Vasudevan SG, Lescar J. 2008. Crystal structure of the NS3 protease-helicase from dengue virus. *J Virol* 82:173–183. <http://dx.doi.org/10.1128/JVI.01788-07>.
  62. Lam AM, Keeney D, Frick DN. 2003. Two novel conserved motifs in the hepatitis C virus NS3 protein critical for helicase action. *J Biol Chem* 278:44514–44524. <http://dx.doi.org/10.1074/jbc.M306444200>.
  63. Cho HS, Ha NC, Kang LW, Chung KM, Back SH, Jang SK, Oh BH. 1998. Crystal structure of RNA helicase from genotype 1b hepatitis C virus. A feasible mechanism of unwinding duplex RNA. *J Biol Chem* 273:15045–15052.
  64. Ishido S, Fujita T, Hotta H. 1998. Complex formation of NS5B with NS3 and NS4A proteins of hepatitis C virus. *Biochem Biophys Res Commun* 244:35–40. <http://dx.doi.org/10.1006/bbrc.1998.8202>.
  65. Kwong AD, Rao BG, Jeang KT. 2005. Viral and cellular RNA helicases as antiviral targets. *Nat Rev Drug Discov* 4:845–853. <http://dx.doi.org/10.1038/nrd1853>.
  66. Mastrangelo E, Bolognesi M, Milani M. 2012. Flaviviral helicase: insights into the mechanism of action of a motor protein. *Biochem Biophys Res Commun* 417:84–87. <http://dx.doi.org/10.1016/j.bbrc.2011.11.060>.
  67. Laine E, Martinez L, Ladant D, Malliavin T, Blondel A. 2012. Molecular motions as a drug target: mechanistic simulations of anthrax toxin edema factor function led to the discovery of novel allosteric inhibitors. *Toxins (Basel)* 4:580–604. <http://dx.doi.org/10.3390/toxins4080580>.